Atomic parity violation measurements in the highly forbidden 6S 1/2-7S1/2 caesium transition. - I. Theoretical analysis, procedure and apparatus

M. A. Bouchiat, J. Guena, L. Pottier

J. Physique **46** (1985) 1897-1924 NOVEMBRE **1985**, PAGE 1897

Classification
Physics Abstracts
35.10W — 35.10D — 32.80 — 32.60

Atomic parity violation measurements in the highly forbidden $6S_{1/2}$-$7S_{1/2}$ caesium transition. I. Theoretical analysis, procedure and apparatus

M. A. Bouchiat, J. Guena and L. Pottier

Laboratoire de Spectroscopie Hertzienne de l'E.N.S. (*) 24, rue Lhomond, 75231 Paris Cedex 05, France

(*Reçu le 9 mai 1985, accepté le 5 juillet 1985*)

Résumé. — Cet article est la première partie d'une présentation détaillée des mesures de violation de parité réalisées sur deux composantes hyperfines de la transition très interdite 6S-7S de l'atome de césium. Lors de l'excitation par un faisceau laser polarisé circulairement dans un champ électrique statique il y a interférence entre une amplitude électromagnétique induite par le champ et l'amplitude induite par l'interaction faible. Cette interférence engendre dans la polarisation électronique de l'état 7S une contribution qui se comporte comme un vecteur polaire lorsqu'on inverse la chiralité de l'expérience. En principe seule cette contribution est observée dans la direction d'observation choisie. On la détecte par l'intermédiaire du taux de polarisation circulaire de la fluorescence 7S-$6P_{1/2}$. Par effet Hanle dans un champ magnétique appliqué périodiquement, on observe de la même manière la contribution conservant la parité, ce qui permet de calibrer l'expérience. Le résultat final est le rapport Im E_1^{pv}/β de l'amplitude violant la parité à la polarisabilité vectorielle. Notre valeur est ($-$ 1,56 $\pm$ 0,17 (stat.) $\pm$ 0,12 (syst.)) mV/cm. Ci-après nous donnons les expressions de tous les signaux atomiques disponibles, puis nous décrivons l'appareillage et les méthodes expérimentales.

Abstract. — This paper is the first part of a detailed presentation of parity violation measurements performed in two hfs components of the highly forbidden 6S-7S transition of the Cs atom. Under excitation by a circularly polarized laser in a dc electric field, interference takes place between an electromagnetic amplitude induced by the field and the parity-violating amplitude induced by weak interactions. This interference gives rise in the electronic polarization of the 7S state to a contribution which behaves like a *vector* when the handedness of the experiment is reversed. In principle, only this contribution is observed in the chosen direction of observation. Detection proceeds through the circular polarization ratio of the 7S-$6P_{1/2}$ fluorescence. By Hanle effect in a magnetic field applied periodically, the parity-conserving contribution is observed in the same way and used to calibrate the experiment. The final result is the ratio Im E_1^{pv}/β of the parity-violating amplitude to the vector polarizability. Our value is ($-$ 1.56 $\pm$ 0.17 (stat.) $\pm$ 0.12 (syst.)) mV/cm. In what follows, we give the formulae for all available atomic signals and describe the apparatus and procedures.

Introduction.

This paper is an attempt at a complete description of our experimental observations of parity violation in the caesium atom. In addition to outlining a logical framework to collect our partial publications of the past years, it endeavours to describe all aspects of the experiment left in the background so far.

Parity violation (PV) in stable atoms is predicted in many unified gauge theories of electromagnetic and weak interactions — in particular in the standard model [1] — where the « weak neutral current » associated with the exchange of weak neutral bosons is the sum of a vector and of an axial part. Despite already abundant experimental support for the standard model in high-energy physics, quantitative confirmation from atomic physics is valuable [2]. The main reason is that atomic PV experiments test very low momentum transfer values ($\sim$ a few MeV/c) and are sensitive to combinations of coupling constants not yet determined in high energy experiments. In our case the measured quantity is the PV electric dipole amplitude of the highly forbidden $6S_{1/2}$-$7S_{1/2}$ transition of the caesium atom. Using a theoretical

(*) Associé au CNRS.

model of this atom, our result provides a value of the « weak vector charge » of the caesium nucleus : $Q_W = -67 \pm 10$ ([1]). The prediction of the standard model ($Q_W = -68.6 \pm 3$ for $\sin^2 \theta(M_W) = 0.215 \pm 0.014$; radiative corrections included) turns out to agree quantitatively with our result.

In designing and realizing this experiment, our primary concern has been the reliability of the experimental results as well as of their interpretation. In choosing caesium ($Z = 55$), as suggested in 1973 [3], we have accepted some sacrifice regarding the size of the expected effects (approximately $\propto Z^3$ [4]) in favour of greater theoretical reliability associated with the nearly one-electron structure. In spite of painfully small counting rates, we have chosen a highly forbidden transition, in order to reduce the risk that purely electromagnetic effects mimic the electroweak PV effect in case of experimental imperfections. We have chosen to detect a polarized quantity induced by an external field introducing a new preferred direction. Because of its specific symmetry, such a quantity is free from any background, since collisional or molecular processes are isotropic on the average. Prior to the PV measurements all sources of possible systematic effects have been reduced so that no significant correction had to be applied to the raw data. The overall systematic uncertainty is estimated at 8 % of the observed effect. Parity violation has been observed in two experiments [5, 6] involving different physical quantities and using control methods different for most systematic effects : the two results (with respectively 6 and 7 σ statistical accuracy) are in quantitative agreement. Finally to test the theoretical model of caesium atom as well as our understanding of the 6S-7S transition, we have measured many parameters of this transition, and compared them with the predictions of the model. The deviation never exceeds 5 %.

To say that « parity is violated » means that the laws of physics — in practice, the laws of weak interactions — violate mirror symmetry. To test parity violation, an experiment is performed in a right-handed and in a left-handed configuration that are images of one another in some mirror. If the corresponding results are *not* images of one another in this mirror, parity is violated. The size of the relative *right-left asymmetry* measures the amount of parity violation. In the case of our experiment, the handedness of the configuration is embodied in the right or left circular polarization of the laser beam which excites the atomic transition. The measured quantity is a component of the electronic polarization of the upper state. When the experimental configuration is replaced by its mirror image, this component is replaced by the *opposite* of its image, i.e. behaves like a vector instead of an axial.

([1]) Statistical, systematic and theoretical uncertainties have been added quadratically.

Reviews of observations of PV in other heavy atoms : Bi, Pb and Tl, can be found in reference [7]. In Bi the observed physical quantity is parity-violating optical rotation in an *allowed* M_1 transition. Initial discrepancies among the Bi results [8-10] have subsequently been reduced [9, 11-13]. The theoretical interpretation, difficult in view of the complex atomic structure, leads to results in qualitative agreement with the standard model. PV optical rotation has also been observed in Pb [14]. In Tl the transition is highly forbidden, like in Cs. The initial 3 σ result [15] has been recently followed by a 7 σ measurement [16], both more accurate and affected by a much smaller systematic correction. For a quantitative interpretation, a direct empirical determination of the parity-conserving amplitude used for calibration is now in progress [16]. Finally caesium remains so far the simplest atom in which an electroweak interference effect has been measured.

For practical reasons the present work will be published in three parts. In the present first part, section 1 introduces the physical parameters of the highly forbidden transition used in this experiment. It also gives the theoretical expressions of the detected signals. Section 2 describes the apparatus. The second part will be devoted to the delicate but crucial problem of systematic effects. The third part will describe data acquisition and processing, and analyse the results and their implications. To simplify the text, technical details are systematically relegated to appendices. References to our previous partial publications avoid repetitions whenever possible.

1. Characteristic features of the transition. Theoretical analysis.

In this section our aim is to present a theoretical analysis of the atomic phenomena involved in the 6S-7S transition of caesium used in the parity violation experiment. First we define the relevant physical parameters involved in the transition amplitude. We indicate their magnitude, now determined experimentally but also predicted theoretically. The agreement at the level of a few per cent is a significant indication of the reliability of the atomic calculations in caesium. A simple formalism allows one to compute, in terms of the transition parameters, all physical quantities observable in a given experimental configuration. We discuss the most important features of the results and emphasize criteria permitting discrimination of the parity violating (PV) signal against the parity conserving (PC) signals. Although the parity experiment is performed in zero magnetic field we were led to consider also the effects of an external dc magnetic field. A detailed analysis in a general configuration is given in appendices A ($H = 0$) and B ($H \neq 0$). The physical significance of the results is in the text.

Table I. — *Parameters illustrating the unusual forbidden character of the* 6S-7S *single-photon caesium transition in zero electric field. The quoted values are deduced from experiment. They turn out to be comparable to what is expected for the still unobserved* 1S-2S *transition in hydrogen.*

	Cs $6S_{1/2}$ - $7S_{1/2}$ (experiment)	H $1S_{1/2}$ - $2S_{1/2}$ (theory)
Magnetic dipole amplitude M_1	$(-42.3 \pm 1.8)\,10^{-6}\,\lvert\mu_B/c\rvert$	$7.4 \times 10^{-6}\,\lvert\mu_B/c\rvert$
hf contribution to M_1	$(-8.1 \pm 0.5)\,10^{-6}\,\lvert\mu_B/c\rvert$	$-2.0 \times 10^{-7}\,\lvert\mu_B/c\rvert$
Oscillator strength	4.0×10^{-15}	4.5×10^{-16}
Absorption cross section (*)	3.2×10^{-26} cm^2	
Absorption length at 10 mtorr (*)	1.4×10^{6} km	
7S → 6S decay rate	$(1.07 \times 10^{6}\ \mathrm{s})^{-1}$	$(4 \times 10^{6}\ \mathrm{s})^{-1}$

(*) Computed at the peak of the Doppler-broadened absorption curve for the 4 → 4 hfs component at 160 °C.

1.1 THE FOUR TRANSITION AMPLITUDES AND THE TRANSITION MATRIX. — The single-photon 6S-7S transition is a quite unusual transition, in particular with respect to its extremely high degree of forbiddenness (see Table I). Its magnetic dipole (M_1) amplitude is considerably smaller than a normal M_1 amplitude. As will be shown hereafter, this results in larger PV right-left asymmetries. Yet this transition is especially simple since it connects two S states of a single valence electron, and involves only a change of the principal quantum number.

We use natural caesium, which contains only one isotope $^{55}_{133}$Cs ($I = 7/2$). Each $S_{1/2}$ state splits into a hyperfine doublet with $F = 3$ or 4. The transition is thus composed of 4 hfs components. The relevant energy levels are shown in figure 1. The first PV measurement was performed in the $4 \to 4$ ($\Delta F = 0$) component, the second in the $3 \to 4$ ($\Delta F = 1$) component. In many respects the two measurements constitute two different experiments. Throughout the text it will be convenient to refer to each of them by a short expression, Exp. 1 and Exp. 2 respectively. Between two $S_{1/2}$ states the only multipole amplitude permitted by the parity selection rule is the magnetic dipole amplitude. When the Cs atom is placed in an external dc electric field, Stark mixing between states of different parity allows in addition the existence of an induced electric dipole amplitude. Furthermore the existence of a PV term in the atomic Hamiltonian due to the weak electron-nucleus interaction, leads to a parity-violating electric dipole amplitude. These 3 contributions of different natures are now examined.

1.1.1 *Magnetic dipole amplitude(s).* — Between two different S states the M_1 amplitude vanishes in first approximation. Yet relativistic effects such as the combined effect of core excitation and spin-orbit coupling lead to a non-zero magnetic dipole amplitude M_1 equal to a fraction of $10^{-4}\,\lvert\mu_B/c\rvert$ [4, 17]. Furthermore the hyperfine interaction mixes S states of different principal quantum number, giving rise to a second magnetic dipole amplitude M_1^{hf} ($F' - F$) proportional to the difference $F' - F$ of the hf quantum numbers of the two sublevels involved in the transition [4]. The total amplitude M_1' defined by :

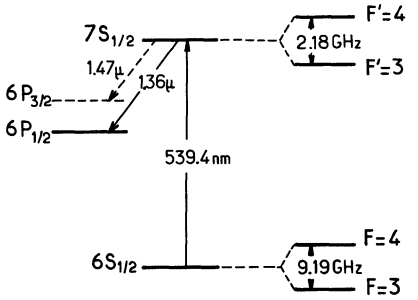

Fig. 1. — Energy levels of natural caesium ($I = 7/2$) involved in this experiment.

$$\left\langle 7S\,F'\,m' \left| \frac{\boldsymbol{\mu}}{c} \right| 6S\,Fm \right\rangle = M_1' \langle F'\,m' \,|\, \boldsymbol{\sigma} \,|\, Fm \rangle \quad (1.1)$$

(where $\boldsymbol{\sigma}$ is the Pauli operator for the electronic spin), is thus given by :

$$M_1' = M_1 + (F' - F)\,M_1^{hf}. \quad (1.2)$$

Since M_1 originates in many-body effects associated with the magnetic polarization of the core, an accurate computation is quite delicate. The most complete calculation at present yields $M_1 = -56 \times 10^{-6}\,\lvert\mu_B/c\rvert$ [18]. On the other hand M_1^{hf} can be predicted much more simply and reliably. Perturbing the states to first order by the hyperfine interaction yields :

$$M_1^{hf} = -[(\Delta W_{6S}^{hf} \cdot \Delta W_{7S}^{hf})^{1/2}/(E_{7S} - E_{6S})] \times \lvert\mu_B/c\rvert$$
$$= -8.06 \times 10^{-6}\,\lvert\mu_B/c\rvert. \quad (1.3)$$

Available experimental values [19, 20, 21] resulting from independent measurements agree together :

$$\left.\begin{aligned} M_1 &= (-42.3 \pm 1.8) \times 10^{-6}\,\lvert\mu_B/c\rvert, \\ M_1^{hf} &= (-8.1 \pm 0.5) \times 10^{-6}\,\lvert\mu_B/c\rvert. \end{aligned}\right\} \quad (1.4)$$

In equation (1.3), many-body effects between electrons in the hyperfine interaction are omitted. From the agreement with the experimental value (1.4) we can conclude that these effects are of limited importance. For a more detailed discussion see reference [19].

1.1.2 *Electric dipole amplitudes.* — The electric dipole operator $\mathbf{d} = -|e| \sum_{k=1}^{Z} \mathbf{r}_k$ acquires non-zero matrix elements between the two S states, when these are perturbed by the static electric field **E** or by the parity-violating electron-nucleus interaction. Symmetry considerations show [22] that these matrix elements are of the following form :

$$\langle 7\tilde{S}_{1/2}\, m'_S \,|\, \mathbf{d} \,|\, 6\tilde{S}_{1/2}\, m_S \rangle = \\ = \langle 1/2\, m'_S \,|\, -\alpha \mathbf{E}\, \mathbb{1} - i\beta\boldsymbol{\sigma} \times \mathbf{E} - i\, \mathrm{Im}\, E_1^{pv}\, \boldsymbol{\sigma} \,|\, 1/2\, m_S \rangle , \quad (1.5)$$

where $\mathbb{1}$ is the unit 2 × 2 matrix. Time reversal invariance implies that the coefficients α, β and $\mathrm{Im}\, E_1^{pv}$ thus defined are real (2). The scalar operator $\alpha \mathbf{E}\mathbb{1}$ can only connect states of same total angular momentum F. The coefficients α and β are called the scalar and vector polarizabilities of the transition. The last contribution involving the matrix element of the electron spin behaves under reflection like an axial. This is a PV manifestation since **d** is a pure vector.

The quantity $\mathrm{Im}\, E_1^{pv}$ is the product of two factors : a purely electroweak one, and a purely atomic one. The electroweak factor is called the « weak charge » Q_W of the caesium nucleus. We assume hereafter $Q_W = -68.6$, the value predicted by the standard electroweak model including radiative corrections [24] and using $\sin^2\theta = 0.215$ for the renormalized weak interaction mixing angle. The atomic factor has been computed, as well as α, β and other parameters of the Cs atom, using the semi-empirical Norcross potential and an electric dipole operator corrected for shielding [23]. Three other complete calculations [25, 26, 27] predict the atomic factor in $\mathrm{Im}\, E_1^{pv}$, but neither α nor β. They are first-principle calculations starting from Dirac-Hartree-Fock wavefunctions. They include many-body effects like modification of the PV interaction by core polarization, shielding of the radiation field by core polarization, and correlation effects on valence orbitals. (In the model using the Norcross potential, the last two effects are incorporated in a semi-empirical way.) The results, shown in table II, differ by less than ± 10 % from the semi-empirical prediction.

There is no direct experimental determination of α and β. But as first suggested by J. Hoffnagle *et al.* [28], it is possible to obtain a rather accurate semi-empirical determination of α from the empirical knowledge of only 4 oscillator strengths. (Two of them are deduced using the optical hook method calibrated by $6P_{3/2}$ lifetime measurements [29], the two others from 7S lifetime [30] and 7S Stark-shift [31] measurements.) This method leads to the result (3) :

$$\alpha_{se} = (-265 \pm 5)\, a_0^3 \quad (1.6)$$

where 1 % uncertainty for the method has been added to the 1 % experimental uncertainty.

In addition the ratio α/β can be directly measured fairly accurately from the hyperfine absorption profile monitored by fluorescence as indicated in § 1.2.1 and shown in figure 2. Our result [32] which agrees

Table II. — *Theoretical predictions of* $\mathrm{Im}\, E_1^{pv}$ *from the most complete atomic calculations, with* $Q_W = -68.6$ *(value obtained from the standard electroweak model with* $\sin^2\theta = 0.215$ *and including radiative corrections* [24]).

		$\mathrm{Im}\, E_1^{pv} (10^{-11} \,|e|\, a_0)$
Semi-empirical calculation	Bouchiat *et al.* [23]	0.85 ± 0.09
First principle	Das *et al.* [25]	0.93
	Dzuba *et al.* [26]	0.77 ± 0.03
	Märtensson [27]	0.78

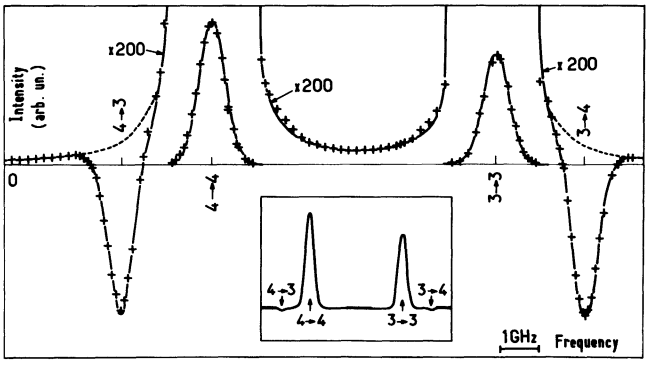

Fig. 2. — Hfs profile of the Stark-induced 6S-7S Cs transition. Rotation of the linear polarization ε of the laser beam generates in the fluorescence intensity $\mathcal{F}_u$ (see Eq. (1.12)) a modulation which amplitude, measured by lock-in detection, is plotted *versus* the laser frequency : (+) experimental points; solid line : Voigt fit. E = 100 V/cm, except in the magnified regions measured at E = 1 000 V/cm and rescaled at E = 100 V/cm.

(2) α, β and $\mathrm{Im}\, E_1^{pv}$ as defined by equation (1.5) are respectively identical with $\alpha(7, 6) = \alpha(6, 7)$, $\beta(7, 6) = -\beta(6, 7)$ and $\mathrm{Im}\, E_1^{pv}(7, 6) = -\mathrm{Im}\, E_1^{pv}(6, 7)$ defined in references [22, 23].

(3) In quoting polarizability values throughout we comply with the traditional definition $E = q/r^2$ for the electric field of a point charge q at distance r. Then $e/a_0^2 = 5.1423 \times 10^9$ V/cm.

with two other independent ones [33, 34] gives :

$$\alpha/\beta = -9.90 \pm 0.10. \quad (1.7)$$

Combined with (1.6), this yields the semi-empirical value :

$$\beta_{se} = (26.8 \pm 0.8)\, a_0^3. \quad (1.8)$$

Examination of table III allows to conclude that the largest discrepancy between experiment and semi-empirical theory does not exceed 5 %. Table III also shows the comparison between experiment and theory for other parameters chosen to test the semi-empirical computation more thoroughly.

1.1.3 *The transition matrix.* — The interaction Hamiltonian of the atom with a resonant laser field of complex polarization $\boldsymbol{\varepsilon}$ and of propagation direction $\hat{\mathbf{k}}$ (a unit vector) is, in the dipole approximation :

$$\mathcal{H} \propto -\mathbf{d}\cdot\boldsymbol{\varepsilon} - \frac{\boldsymbol{\mu}}{c}\cdot(\hat{\mathbf{k}}\times\boldsymbol{\varepsilon}).$$

The transition amplitude between two hyperfine sublevels :

$$\left\langle 7S\, F'\, m_{F'} \left| -\mathbf{d}\cdot\boldsymbol{\varepsilon} - \frac{\boldsymbol{\mu}}{c}\cdot(\hat{\mathbf{k}}\times\boldsymbol{\varepsilon}) \right| 6S\, F m_F \right\rangle = T_{F' m_{F'} F m_F} \quad (1.9)$$

can be considered as the element of a matrix T, called *transition matrix*, operating only on spin variables. From equations (1.1), (1.2) and (1.5) it results that :

$$T = \alpha\mathbf{E}\cdot\boldsymbol{\varepsilon}\,\mathbb{1} + i\beta\boldsymbol{\sigma}\times\mathbf{E}\cdot\boldsymbol{\varepsilon} - [M_1 + (F'-F)\,M_1^{hf}]\times \times\boldsymbol{\sigma}\times\hat{\mathbf{k}}\cdot\boldsymbol{\varepsilon} + i\,\mathrm{Im}\,E_1^{pv}\,\boldsymbol{\sigma}.\boldsymbol{\varepsilon}. \quad (1.10)$$

The relative magnitudes of the parity-conserving terms, now known from several independent measurements, are summarized in table IV. In practical experimental conditions the induced electric dipole is dominant. The determination of Im E_1^{pv} was the ultimate goal of the experiment. Within the standard electroweak model the theoretical predictions of table II lead to expect $2\,\mathrm{Im}\,E_1^{pv}/M_1 \simeq 10^{-4}$.

All observable physical quantities involve squared matrix elements of T. They contain interference terms between the four dipoles associated with α, β, M_1' and E_1^{pv}. Terms linear in $\boldsymbol{\sigma}$ contribute to the electronic polarization in the final state, terms quadratic in $\boldsymbol{\sigma}$ contribute to both the population and the polarization of the final state. The complete computation of the electronic polarization of the 7S state in the most general configuration is necessary for a complete understanding of our PV experiment. Since the details may look rather tedious and are unnecessary to understand the philosophy of the experiment, we present the computation in appendix A. In the next section we analyse the results.

1.2 THE ATOMIC SIGNALS IN ZERO MAGNETIC FIELD. — As already said in the introduction the basic principle of our parity experiment consists in testing the symmetry properties of the 7S state under a mirror reflec-

Table III. — *Atomic parameters of the* 6S-7S *caesium transition and of the* 6S *and* 7S *states. Comparison between experiment and theoretical predictions obtained with the semi-empirical Norcross potential and an electric dipole operator corrected for shielding* [23].

	Exp.	Theor.	$\frac{\text{th.} - \text{exp.}}{\text{th.}}$
Lifetime τ_{7S} (ns)	48.5 ± 0.5 [30]	48.35	< exp. unc.
Diagonal α_{Cs} (a_0^3)	402 ± 8 [36]	398.4	< exp. unc.
Polarizabilities $(\alpha_{77}-\alpha_{66})$ (a_0^3)	− 5 709 ± 21 [31]	− 5 807	1.7×10^{-2}
Off-diagonal scalar α (a_0^3)	− 265 ± 5 (*)	− 257.7	-2.8×10^{-2}
and vector β (a_0^3)	26.8 ± 0.8	27.3	< exp. unc.
Polarizabilities α/β	− 9.9 ± 0.1 [32-34]	− 9.43	-5.0×10^{-2}
Hyperfine Splittings H_{66}^{hf} (MHz)	9 192 [35]	9 655	4.8×10^{-2}
H_{77}^{hf} (MHz)	2 184 [34]	2 285	4.4×10^{-2}
Test of the factorization rule $\frac{H_{76}^{hf}}{(H_{77}^{hf}\cdot H_{66}^{hf})^{1/2}}$	1.002 ± 0.05 (**)	1	< exp. unc.

(*) Semi-empirical value (see text).
(**) Obtained using the value of M_1^{hf} quoted in text.

Table IV. — *Relative magnitudes of the* 6S → 7S *parameters from various experiments.*

	Paris [32, 19, 21]	Zurich [33]	Michigan [34, 20]
α/β	− 9.90 ± 0.10	− 9.91 ± 0.11	− 9.80 ± 0.12
M_1/β (V/cm)	− 29.59 ± 0.47	− 26.2 ± 1.7	− 29.73 ± 0.34
M_1/α (V/cm)	2.99 ± 0.06	2.57 ± 0.16	3.03 ± 0.05
M_1^{hf}/M_1	0.191 ± 0.004	0.31 ± 0.03 (*)	0.180 ± 0.013

(*) The discrepancy in M_1^{hf}/M_1 between [33] and the other consistent results [20, 21], can probably be ascribed to the large size and complicated structure of the background present in the Zurich experiment.

tion. One simple way to perform such a reflection is to reverse the circular polarization of the incident light from right to left. Therefore this circular polarization ξ (also called photon helicity) plays hereafter an essential role. In the definition :

$$\xi = \mathrm{Im}\,(\boldsymbol{\varepsilon}^* \times \boldsymbol{\varepsilon}\cdot\hat{\mathbf{k}})/|\,\boldsymbol{\varepsilon}\,|^2 \qquad (1.11)$$

its pseudoscalar nature is apparent : ξ changes its sign whenever a mirror symmetry is performed on the experimental configuration.

A convenient way to probe the 7S excited state consists in monitoring the fluorescence light emitted in the $7S_{1/2}$-$6P_{1/2}$ decay at 1.36 μ (Fig. 1). Since the hyperfine structure of the $7S_{1/2}$-$6P_{1/2}$ line is not resolved, the intensity and polarization of the fluorescence light depend only on the population and electronic orientation of the 7S state. This will now be considered in detail.

1.2.1 *The upper state population and the « unpolarized fluorescence signal ».* — In the population of the upper state we expect to find essentially contributions associated with the squares of the matrix elements of each dipole : $\alpha^2\,|\,\mathbf{E}\cdot\boldsymbol{\varepsilon}\,|^2$ (for $\Delta F = 0$ transitions only), $\beta^2\,|\,\mathbf{E}\times\boldsymbol{\varepsilon}\,|^2$, $M_1'^2$ and $(\mathrm{Im}\,E_1^{pv})^2$. This last term will be ignored later on since it is so minute. We also expect to find interference terms involving two spin-dependent amplitudes. For reasons connected with their relative phase (implied by time reversal invariance) there is only one such interference term : $\xi M_1'\,\mathrm{Im}\,E_1^{pv}$. Such a pseudoscalar contribution represents a parity-violating circular dichroism. In principle it could lead to experimental evidence of the PV interaction (as suggested earlier [3]). However this is not the effect which is searched for in the experiments discussed here. Furthermore our experimental conditions (beam multipass) tend to reduce its contribution considerably. So we ignore this term hereafter.

We measure the intensity of the $7S_{1/2}$-$6P_{1/2}$ fluorescence, proportional to the population of the $7S_{1/2}$ state. To recall that this intensity can be measured without any polarization analyser, we call it the « *unpolarized fluorescence signal* » $\mathcal{F}_u$. Its expression is given by (A.20) in appendix A :

$$\mathcal{F}_u = n_{F'}[\delta_{FF'}\,\alpha^2\,|\,\mathbf{E}\cdot\boldsymbol{\varepsilon}\,|^2 + h_{FF'}(\beta^2\,|\,\mathbf{E}\times\boldsymbol{\varepsilon}\,|^2 + M_1'^2\,|\,\boldsymbol{\varepsilon}\,|^2)] \qquad (1.12)$$

with $\delta_{FF'} = 1$ if $F = F'$ and 0 if $F \neq F'$; the other nuclear-spin dependent coefficients are defined in equations (A.8 and 5). Both Stark-induced contributions strongly depend on the relative orientation of the laser polarization with respect to the electric field **E**. The favoured direction of **E** labels the Stark-induced terms with a particular symmetry. This proves to be very useful to distinguish the atomic fluorescence from collisional or molecular effects, isotropic on the average. This results in the absence of background illustrated by figure 2. In this measurement the laser polarization $\boldsymbol{\varepsilon}$ is linear and rotates at a fixed frequency. In the fluorescence intensity, terms proportional to $\alpha^2\,|\,\mathbf{E}\cdot\boldsymbol{\varepsilon}\,|^2$ and $\beta^2\,|\,\mathbf{E}\times\boldsymbol{\varepsilon}\,|^2$ become modulated. The amplitude of this modulation is plotted in figure 2 *versus* the laser frequency. Interpretation of the entire spectral profile presents no difficulty [32]. Background turns out to be absent at the level of 10^{-3} of the smaller lines. The intensity ratios of the 4 hfs components are consistent with the predictions (1.12), and lead to the determination of $(\alpha/\beta)^2$ quoted above (Eq. (1.7)). In addition the possibility of accurately checking the absence of background is important for the parity experiment since this property extends to any physical quantity which depends on the electric field in such a way that its average vanishes when the field is distributed isotropically (like the effective field in a collisional or molecular process).

On the contrary, all directions of $\boldsymbol{\varepsilon}$ play the same rôle for the $M_1'^2$ term. Consequently it is delicate in zero electric field to extract the atomic resonances from the background, when the detected physical quantity is $\mathcal{F}_u$ [33]. The background originates partly in collision-induced absorption and partly in a complex molecular spectrum of loosely bound Cs_2 dimers.

Our parity experiment avoids this difficulty by performing the experiment in an electric field and modulating the direction of the exciting light polarization. The background and the $M_1'^2$ terms staying both unmodulated do not affect directly the detected signals. Yet they have been included in the very detailed analysis of systematic effects (part II).

1.2.2 *The upper state polarization and the « polarized fluorescence signal ».* — There is a simple relation between the electronic polarization $\mathbf{P} = (2/\hbar) \langle \mathbf{S} \rangle$ in the 7S state and the helicity of the fluorescence light emitted in any direction $\hat{\mathbf{k}}_f$: the helicity is equal to the projection $\mathbf{P}\cdot\hat{\mathbf{k}}_f$ on the considered direction. In our experiment the fluorescence light is passed through a polarization analyser of modulated helicity ξ_f. The transmitted intensity contains a modulation :

$$\mathcal{F}_p = \xi_f\cdot(\mathbf{P}\cdot\hat{\mathbf{k}}_f)\,\mathcal{F}_u\,, \tag{1.13}$$

hereafter called the *polarized fluorescence signal.*

We expect various contributions to the electronic polarization of the excited state and thereby also to $\mathcal{F}_p$. They can originate in interference between the spin-independent amplitude $\alpha\mathbf{E}\cdot\boldsymbol{\varepsilon}$ and the various spin-dependent ones associated with M_1', β and E_1^{pv} respectively. But they can also arise from interference between two spin-dependent amplitudes : $\beta E - M_1'$, $\beta E - \beta E$, $M_1' - M_1'$, etc... The complete expression of $\mathcal{F}_p$, obtained in appendix A (Eqs. (A.15) to (A.19)) is :

$$\mathcal{F}_p = \mathcal{F}^{pv} + \mathcal{F}^{(2)} + \mathcal{F}^{(1)} + \mathcal{F}^{(0)} \tag{1.14}$$

with :

$$\mathcal{F}^{pv} = \mathcal{F}_u\,\mathbf{P}^{pv}\cdot\xi_f\,\hat{\mathbf{k}}_f \propto \mathrm{Im}\,E_1^{pv}(\delta_{FF'}\,\alpha + g_{FF'}\,\beta)\,\mathbf{E}\times\xi\hat{\mathbf{k}}\cdot\xi_f\,\hat{\mathbf{k}}_f \tag{1.15}$$

$$\mathcal{F}^{(2)} = \mathcal{F}_u\,\mathbf{P}^{(2)}\cdot\xi_f\,\hat{\mathbf{k}}_f \propto [-\delta_{FF'}\,\alpha\beta E^2\,\xi\hat{\mathbf{k}} + (\delta_{FF'}\,\alpha + g_{FF'}\,\beta)\,(\mathbf{E}\cdot\xi\hat{\mathbf{k}})\,\beta\mathbf{E}]\cdot\xi_f\,\hat{\mathbf{k}}_f \tag{1.16}$$

$$\mathcal{F}^{(1)} = \mathcal{F}_u\,\mathbf{P}^{(1)}\cdot\xi_f\,\hat{\mathbf{k}}_f \propto M_1'\,2\,\mathrm{Re}\,[\delta_{FF'}\,\alpha(\hat{\boldsymbol{\varepsilon}}\cdot\mathbf{E})\,(\hat{\boldsymbol{\varepsilon}}^*\times\hat{\mathbf{k}}) + g_{FF'}\,\beta\,(\hat{\mathbf{k}}\times\hat{\boldsymbol{\varepsilon}}\cdot\mathbf{E})\,\hat{\boldsymbol{\varepsilon}}^*]\cdot\xi_f\,\hat{\mathbf{k}}_f \tag{1.17}$$

$$\mathcal{F}^{(0)} = \mathcal{F}_u\,\mathbf{P}^{(0)}\cdot\xi_f\,\hat{\mathbf{k}}_f \propto g_{FF'}\,M_1'^2\,\xi\hat{\mathbf{k}}\cdot\xi_f\,\hat{\mathbf{k}}_f \tag{1.18}$$

up to a common normalization factor. Here $g_{FF'} = g_F$ if $F = F'$, and $1 - g_{F'}$ if $F \neq F'$, with $g_{F'} = 2(F' - I)/(2I + 1)$; $\hat{\boldsymbol{\varepsilon}} = \boldsymbol{\varepsilon}/|\,\boldsymbol{\varepsilon}\,|$ is the unit polarization vector.

Equations (1.13)-(1.18) imply for the electronic polarization a decomposition :

$$\mathbf{P} = \mathbf{P}^{pv} + \mathbf{P}^{(2)} + \mathbf{P}^{(1)} + \mathbf{P}^{(0)}$$

in four contributions, whose physical interpretation is now examined.

(i) $\mathbf{P}^{pv}$ (Eq. (1.15)) is the parity-violating component. It is created in the direction $\mathbf{E}\times\xi\hat{\mathbf{k}}$ by interference between the PV amplitude $\mathrm{Im}\,E_1^{pv}$ and the Stark-induced amplitudes αE and/or βE (depending on whether $\Delta F = 0$ or ± 1), when the helicity ξ of the laser polarization is non zero. The corresponding fluorescence signal $\mathcal{F}^{pv} \propto \mathbf{E}\times\xi\hat{\mathbf{k}}\cdot\xi_f\,\hat{\mathbf{k}}_f$ is a *pseudoscalar*, which clearly manifests a parity violation. It has a specific behaviour (it is odd) under reversal of each experimental parameter ξ, $\hat{\mathbf{k}}$, $\mathbf{E}$, ξ_f or $\hat{\mathbf{k}}_f$. $\mathcal{F}^{pv}$ is the searched for (and observed) parity violation signal. On the contrary, the last three terms in $\mathcal{F}_p$ are scalars associated with the PC components of the electronic polarization, $\mathbf{P}^{(2)}$, $\mathbf{P}^{(1)}$ and $\mathbf{P}^{(0)}$.

(ii) Component $\mathbf{P}^{(0)}$ does not originate in an interference but in direct excitation of the M_1' amplitude. It is created along the angular momentum $\xi\hat{\mathbf{k}}$ of the incident photons, and is thus orthogonal to $\mathbf{P}^{pv}$. In addition it is unchanged when $\mathbf{E}$ is reversed. So it differs from $\mathbf{P}^{pv}$ by two features (one orthogonality and one reversal). At the field values of the measurements the ratio $P^{pv}/P^{(0)}$ is :

$$\sim \alpha E\,\mathrm{Im}\,E_1^{pv}/g_{F'}\,M_1^2 \simeq 1.3\times 10^{-2}\,, \quad \text{in Exp. 1 } (E = 100\ \mathrm{V/cm})\,,$$

$$\sim \beta E\,\mathrm{Im}\,E_1^{pv}/M_1'^2 \simeq 1.5\times 10^{-2}\,, \quad \text{in Exp. 2 } (E = 600\ \mathrm{V/cm})\,.$$

Note that a suitable choice of the geometry ($\hat{\mathbf{k}}_f \perp \hat{\mathbf{k}}$) can considerably enhance $\mathcal{F}^{pv}/\mathcal{F}^{(0)}$ with respect to $P^{pv}/P^{(0)}$.

(iii) Component $\mathbf{P}^{(2)}$ also involves the angular momentum $\xi\hat{\mathbf{k}}$ of the incident photon. Being created in the ($\mathbf{E}$, $\hat{\mathbf{k}}$) plane, it is thus orthogonal to $\mathbf{P}^{pv}$. It originates in interference between two Stark-induced amplitudes ($\alpha E.\beta E$ and/or $\beta E.\beta E$, depending on whether $\Delta F = 0$ or ± 1) and therefore it is not reversed under reversal of $\mathbf{E}$. Thus, just like $\mathbf{P}^{(0)}$, $\mathbf{P}^{(2)}$ differs from $\mathbf{P}^{pv}$ by also two features. Let us note two contributions in $\mathbf{P}^{(2)}$: the first one, along the beam, is present only in $\Delta F = 0$ hfs components; the second one, along $\mathbf{E}$, is present in all hfs components but vanishes when the Stark field is normal to the laser beam ($\mathbf{E}.\hat{\mathbf{k}} = 0$). In $\Delta F = 0$ transitions the ratio $P^{pv}/P^{(2)}$ is typically given by :

$$\mathrm{Im}\,E_1^{pv}/\beta E \sim 1.5\times 10^{-5}\,, \quad \text{for} \quad E = 100\ \mathrm{V/cm}\,.$$

Again a suitable choice of the geometry ($\hat{\mathbf{k}}_f$ normal to the $\mathbf{E}$, $\hat{\mathbf{k}}$ plane) can considerably enhance $\mathcal{F}^{pv}/\mathcal{F}^{(2)}$ with respect to $P^{pv}/P^{(2)}$.

(iv) The last component $\mathbf{P}^{(1)}$ originates in interference of the magnetic and Stark-induced electric dipoles. Therefore it is odd under reversal of $\mathbf{E}$, just like $\mathbf{P}^{pv}$. But a first essential feature is that $\mathbf{P}^{(1)}$ does not involve the incident helicity ξ, contrary to $\mathbf{P}^{pv}$, $\mathbf{P}^{(2)}$ and $\mathbf{P}^{(0)}$. Instead $\mathbf{P}^{(1)}$ depends on the total intensity and on the linear polarization embodied in $\mathrm{Re}\,[(\boldsymbol{\varepsilon}.\mathbf{E})(\boldsymbol{\varepsilon}^* \times \hat{\mathbf{k}})]$ or $\mathrm{Re}\,[(\hat{\mathbf{k}} \times \boldsymbol{\varepsilon}.\mathbf{E})\,\boldsymbol{\varepsilon}^*]$. The latter dependence is anisotropic, and favours the direction of the projection of $\mathbf{E}$ on a plane normal to $\hat{\mathbf{k}}$. A second important feature of $\mathbf{P}^{(1)}$ is that it reverses when the propagation direction $\hat{\mathbf{k}}$ is reversed without any change in $\boldsymbol{\varepsilon}$. Such a reversal can be realized by normal reflection on a mirror and conserves the longitudinal angular momentum $\xi\hat{\mathbf{k}}$. Thus in contradistinction to $\mathbf{P}^{(1)}$, $\mathbf{P}^{pv}$ (like $\mathbf{P}^{(0)}$ and $\mathbf{P}^{(2)}$) is conserved in this reversal. This provides a second criterium to discriminate $\mathbf{P}^{pv}$ against $\mathbf{P}^{(1)}$. Finally the ratio $\mathcal{F}^{pv}/\mathcal{F}^{(1)}$ remains of the order of

$$P^{pv}/P^{(1)} \sim \mathrm{Im}\, E_1^{pv}/M_1 \sim 0.5 \times 10^{-4}$$

whatever the respective orientations of $\mathbf{E}$, $\hat{\mathbf{k}}$ and $\hat{\mathbf{k}}_f$. This result holds for any hfs component.

The characteristic features of each contribution to the fluorescence signals are summarized in the upper half of table V. Each of the three PC polarized fluorescence signals has been extensively studied in auxiliary experiments with various geometries, and along the 6S-7S hfs profile. The characteristic features have been copiously verified. In particular the absence of background in $\mathcal{F}^{(1)}$ and $\mathcal{F}^{(2)}$ has been observed : i) by exploring their spectral profile; ii) by checking the proportionality to E of the ratio $\mathcal{F}^{(2)}/\mathcal{F}^{(1)}$ [19]. However we must here mention the existence of a small background affecting the E-independent signal $\mathcal{F}^{(0)}$. This background induced by collisions with the atoms of the buffer gas (helium) is independent of $\mathbf{E}$ and associated with an electronic polarization directed along $\xi\hat{\mathbf{k}}$ (see remark at the end of appendix A). Yet it can be distinguished from $\mathcal{F}^{(0)}$ through its non-resonant behaviour *versus* the laser frequency, as well as through its different Hanle effect (appendix B). This small signal too has been studied in detail [21]. It turns out to play a very minor rôle in the complete analysis of the parity experiments (appendix F, in

Table V. — *The fluorescence signals and their characteristics in a general geometrical configuration.*

Fluorescence signals	Interference	Complete signature	Incident polarization involved	Geometrical factor	Behaviour under reversals E	ξ	ξ & $\hat{\mathbf{k}}$	ξ_f	
$\mathcal{F}^{PV}$	$\mathrm{Im}\, E_1^{pv}\,\alpha E$ $\mathrm{Im}\, E_1^{pv}\,\beta E$	$\mathbf{E}\times\xi\hat{\mathbf{k}}\cdot\xi_f\hat{\mathbf{k}}_f$	circ.	$\mathbf{E}\times\hat{\mathbf{k}}\cdot\hat{\mathbf{k}}_f$	−	−	+	−	
$\mathcal{F}^{(0)}$	$M_1'^2$	$\xi\hat{\mathbf{k}}\cdot\xi_f\hat{\mathbf{k}}_f$	circ.	$\hat{\mathbf{k}}\cdot\hat{\mathbf{k}}_f$	+	−	+	−	
$\mathcal{F}^{(2)}$	$\alpha\beta E^2$ $\beta^2 E^2$	$\xi\hat{\mathbf{k}}\cdot\xi_f\hat{\mathbf{k}}_f$ $(\mathbf{E}\cdot\xi\hat{\mathbf{k}})(\mathbf{E}\cdot\xi_f\hat{\mathbf{k}}_f)$	circ.	$\hat{\mathbf{k}}\cdot\hat{\mathbf{k}}_f$ $(\mathbf{E}\cdot\hat{\mathbf{k}})(\mathbf{E}\cdot\hat{\mathbf{k}}_f)$	+	−	+	−	present in $H=0$
$\mathcal{F}^{(1)}$	$M_1'\,\alpha E \leftrightarrow \mathrm{Re}\{\boldsymbol{\varepsilon}\cdot\mathbf{E}(\boldsymbol{\varepsilon}^*\times\hat{\mathbf{k}}\cdot\xi_f\hat{\mathbf{k}}_f)\}$ $M_1'\,\beta E \leftrightarrow \mathrm{Re}\{(\boldsymbol{\varepsilon}\times\mathbf{E}\cdot\hat{\mathbf{k}})\,\boldsymbol{\varepsilon}^*\cdot\xi_f\hat{\mathbf{k}}_f\}$	lin.	$\mathbf{E}\times\hat{\mathbf{k}}\cdot\hat{\mathbf{k}}_f$ $\hat{\mathbf{E}}_\perp\cdot\hat{\mathbf{k}}_f$ (*)	−	+	−	−	
$\mathcal{F}_u$	$\alpha^2 E^2$ $\beta^2 E^2$	$\lvert\boldsymbol{\varepsilon}\cdot\mathbf{E}\rvert^2$ $\lvert\boldsymbol{\varepsilon}\times\mathbf{E}\rvert^2$	lin.		+	+	+	+	
Hanle effect $\mathcal{F}^{(2)}(H_0)+\mathcal{F}^{(0)}(H_0)$	$\alpha\beta E^2$ $M_1'^2$	$\mathbf{H}\times\xi\hat{\mathbf{k}}\cdot\xi_f\hat{\mathbf{k}}_f$	circ.	$\mathbf{H}\times\hat{\mathbf{k}}\cdot\hat{\mathbf{k}}_f$	+	−	+	−	max for $\mathbf{H}//\hat{\mathbf{k}}\times\hat{\mathbf{k}}_f$
hf mixing	$\mathcal{F}_{hf}^{\times}$	$\alpha\beta E^2$	$\mathrm{Re}\{(\boldsymbol{\varepsilon}\cdot\mathbf{E})(\boldsymbol{\varepsilon}^*\times\mathbf{E})\times\mathbf{H}\cdot\xi_f\hat{\mathbf{k}}_f\}$	lin.	$\mathbf{H}\times\hat{\mathbf{k}}\cdot\hat{\mathbf{k}}_f$	+	+	+	−	
	$\mathcal{F}_{hf}$	$\alpha^2 E^2$ $\beta^2 E^2$	$\lvert\boldsymbol{\varepsilon}\cdot\mathbf{E}\rvert^2\,\mathbf{H}\cdot\xi_f\hat{\mathbf{k}}_f$ $\lvert\boldsymbol{\varepsilon}\times\mathbf{E}\rvert^2\,\mathbf{H}\cdot\xi_f\hat{\mathbf{k}}_f$	lin.	$\mathbf{H}\cdot\hat{\mathbf{k}}_f$	+	+	+	−	$\mathbf{H}//\hat{\mathbf{k}}_f$
	$\mathcal{F}_{u,hf}$	$\alpha\beta E^2$	$\mathbf{H}\cdot\xi\hat{\mathbf{k}}$	circ.	$\mathbf{H}\cdot\hat{\mathbf{k}}_f$	+	−	+	+	
	$\mathcal{F}_{hf}^{(1)}$	$M_1'\,\alpha E$ $M_1'\,\beta E$	$\mathbf{H}\cdot\hat{\mathbf{k}}(\mathbf{E}\times\xi\hat{\mathbf{k}}\cdot\xi_f\hat{\mathbf{k}}_f)$	circ.	$\mathbf{H}\cdot\hat{\mathbf{k}}(\mathbf{E}\times\hat{\mathbf{k}}\cdot\hat{\mathbf{k}}_f)$	−	−	−	−	$\mathbf{H}//\hat{\mathbf{k}}$
Hanle effect $\mathcal{F}^{(2)}(H_k)$	$\alpha\beta E^2$ $\beta^2 E^2$	$(\mathbf{H}\times\mathbf{E}\cdot\xi_f\hat{\mathbf{k}}_f)\,\mathbf{E}\cdot\xi\hat{\mathbf{k}}$	circ.	$(\mathbf{H}\cdot\mathbf{E}\times\hat{\mathbf{k}}_f)\,\mathbf{E}\cdot\hat{\mathbf{k}}$	+	−	+	−	H odd

(*) $\hat{\mathbf{E}}_\perp$ represents a unit vector along the $\mathbf{E}$ component normal to $\hat{\mathbf{k}}$.

part II). Studies of $\mathbf{P}^{(1)}$ and of $\mathbf{P}^{(0)}$ in $E = 0$, have yielded precise and independent measurements of M_1 and M_1^{hf} (Eqs. (1.4)). $\mathbf{P}^{(2)}$, by far the largest component whenever $E \neq 0$, is very useful as a standard to calibrate the measurements of all other components and in particular of $\mathbf{P}^{pv}$ (§ 1.3).

1.2.3 *The ideal configuration.* — We are in a position to choose the geometry of the experiment. Ideally the configuration should maximize the PV signal and simultaneously cancel most of the PC signals. The best observation direction $\hat{\mathbf{k}}_f$ to maximize $\mathbf{P}^{pv}$ is along $\mathbf{P}^{pv}$ itself, i.e. transverse to both the beam and the electric field. This direction has the additional advantage of cancelling the fluorescence signals $\mathcal{F}^{(0)}$ and $\mathcal{F}^{(2)}$ (Eqs. (1.18) and (1.16) with $\mathbf{E} \cdot \hat{\mathbf{k}}_f = \hat{\mathbf{k}} \cdot \hat{\mathbf{k}}_f = 0$)

Concerning now the choice of the incident polarization $\boldsymbol{\varepsilon}$, maximizing the PV signal requires either right or left circular polarization ($\xi = \pm 1$). The corresponding configuration is schematized on figure 3a for a given beam propagation direction. Figure 3b shows the image configuration, obtained by reflecting a) in a mirror normal to the laser beam. In our experiment a) and b) constitute the pair of mirror-image configurations on which any parity-violation experiment is based (cf. introduction). In both a) and b) the components $\mathbf{P}^{(0)}$ and $\mathbf{P}^{(2)}$, created along the beam, are unobserved. What is observed is the PV component $\mathbf{P}^{pv}$ to which $\mathbf{P}^{(1)}$ adds in one case and subtracts in the other case. The polarized fluorescence signal detected in either configuration reduces to :

$$\mathcal{F}_p = \pm \mathcal{F}^{(1)} + \mathcal{F}^{pv} \propto$$
$$\propto (\delta_{FF'} \alpha + g_{FF'} \beta) E(\pm M_1' + \xi \operatorname{Im} E_1^{pv}) \xi_f .$$

Using two counterpropagating beams the two configurations can be superimposed (Fig. 3c). The component $\mathbf{P}^{(1)}$ then cancels out, and the only electronic polarization remaining in the detection direction is the PV component $\mathbf{P}^{pv}$. Moreover, while $\mathcal{F}^{(1)}$ vanishes identically, $\mathcal{F}^{pv}$ is doubled. The polarized fluorescence signal now detected is :

$$\mathcal{F}_p = 2\,\mathcal{F}^{pv} \propto 2(\delta_{FF'} \alpha + g_{FF'} \beta) E \operatorname{Im} E_1^{pv} \xi \xi_f .$$

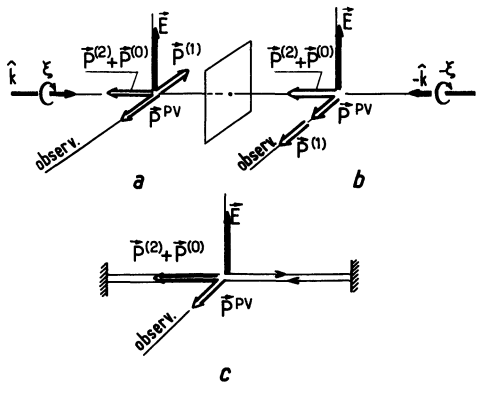

Fig. 3. — Building the ideal experimental configuration : a) and b) : pair of handed configurations, image of one another in a mirror normal to the laser beam ; c) : the ideal configuration, obtained by superposition of a) and b).

The first major advantage of the ideal configuration c) is that *the* PV *signal is in principle detected in total absence of any other polarized fluorescence signal.* This can be rediscovered from simple symmetry considerations. Configuration (c) possesses a symmetry plane, and the direction of observation lies in this plane. Consequently, any observed polarization has to behave like a vector instead of an axial, thus manifesting parity violation. One may also note the invariance of the ideal configuration under still another transformation : a rotation of π around $\mathbf{E}$ followed by time reversal. This implies that a component of $\mathbf{P}$ along $\mathbf{E}$ vanishes identically.

Of course, in practice the real configuration can never exactly coincide with the ideal one. As a result the PC fluorescence signals do not exactly cancel out. However the PV signal in the real configuration still possesses three characteristic features (apparent in Eq. (1.15)) : it is odd under reversal of $\mathbf{E}$, ξ or ξ_f. We have seen in the previous section that each PC signal differs from the PV signal by at least two criteria involving either the geometry of the experiment or these reversals (Table V). Therefore, by reversing in succession the three mentioned parameters and keeping, after each reversal, the odd part of the detected fluorescence signal, we expect the contribution from residual PC effects to be, in the worst case, only second-order small.

A second advantage of the double-pass configuration is that the signal is doubled. In practice the enhancement can be made considerable (about 2 orders of magnitude) by the use of multiple ($\sim$ 70) forward-backward passages of the beam. Let us stress that the use of this very advantageous multipass configuration is possible only because we look for an interference $E_1^{pv} E_1^{ind}$ involving an amplitude E_1^{ind} induced by the electric field. On the contrary $M_1 E_1^{pv}$ interference effects (just as $M_1 E_1^{ind}$ effects) are odd under reversal of the laser beam direction and cancel out in the multipass. Enhancing them instead of cancelling them, would require a ring cavity in which the light wave propagates always in the same direction.

Yet in choosing pure circular polarization we cannot discriminate Stark-induced signals involving the incident linear polarization such as $\mathcal{F}_u$ from the d.c. background. To remedy this, in the real experiment the polarization of the incident beam is not *reversed* from right to left circular, but *modulated* (Sect. 2) in a way which conserves the total polarization degree. So when the circular polarization goes through zero the linear polarization is maximum — in a direction that is modulated too. Thus at the expense of a minor reduction in the rms amplitude of the PV signal we succeed in solving the background

problem. Simultaneously to the PV signal we obtain many other atomic signals. They provide a wealth of information about experimental imperfections, potential sources of systematics (part II).

1.3 ATOMIC SIGNALS IN NON-ZERO MAGNETIC FIELD. — The PV experiment is supposed to be performed in zero magnetic field. However the effects of a magnetic field on the atomic signal have to be understood for at least two reasons :

(i) stray magnetic fields may simulate the PV effect;

(ii) controlled magnetic fields provide new configurations in which new atomic signals appear. These signals have proved useful for calibrating the PV signal and as atomic probes of experimental imperfections (part II). References [37, 38] give a detailed analysis of the new effects arising from M_1'-Stark or Stark-Stark interference in a magnetic field of arbitrary direction. In the PV experiment two classes of effects are involved : hyperfine mixing, and Hanle effect. The lifting of level degeneracy by the magnetic field plays no rôle in practice. (For rigorous expressions see appendix B.)

1.3.1 *Hyperfine mixing effects.* — By hf mixing new terms are created in both the population and the spin polarization of the 7S state. Their relative size is larger in $\Delta F = \pm 1$ components than in $\Delta F = 0$ ones by a factor $\alpha/\beta \approx 10$: the reason is that the scalar amplitude αE becomes allowed in the $\Delta F = \pm 1$ case by hf mixing while it is strictly forbidden by angular momentum conservation when $H = 0$. Therefore these effects played a more important rôle in the $\Delta F = 1$ case (Exp. 2).

In view of the symmetry of the Stark-induced and M_1' dipoles, the direction of the magnetic field with respect to the beam direction, as well as the incident polarization, are important.

(i) New *ξ-dependent* terms appear in both the unpolarized and polarized fluorescence signals when **H** has a component along the beam. Up to a nuclear-spin dependent factor given in appendix B, their respective expressions are :

$$\mathcal{F}_{u,hf} \propto \alpha\beta E^2(\mu_B \mathbf{H}\cdot\xi\hat{\mathbf{k}}/\hbar\omega_{hf}) \qquad (1.19)$$

$$\mathcal{F}^{(1)}_{hf} \propto M_1' \, \alpha\mathbf{E} \times \xi\hat{\mathbf{k}}\cdot\xi_f \hat{\mathbf{k}}_f(\mu_B \mathbf{H}\cdot\hat{\mathbf{k}}/\hbar\omega^*_{hf}) . \qquad (1.20)$$

Here ω_{hf} and ω^*_{hf} are functions of the hf splittings of the 6S and 7S states. For $H \sim 1$G both factors in parentheses are $\sim 10^{-3}$. The first signal describes a circular dichroism (CD). It implies that the Cs vapour does no longer act as a pure linear analyser of the beam polarization, as it does when $H = 0$. ($\mathcal{F}_u$ (Eq. (1.12)) is in that case independent of ξ). We must be aware of this when we make use of $\mathcal{F}_u$ to probe the beam polarization imperfections (part II). This atomic CD can be distinguished from stray CD or birefringence in the optics by comparing different hfs lines : the atomic CD signals have opposite signs for $F' = 3$ and $F' = 4$ (Eq. (B.8)). On the other hand, in a large known magnetic field, this ξ-dependent signal provides a convenient method to test imperfections in the incident helicity. This was used during Exp. 2 performed on the $3 \to 4$ component where the CD is particularly large (part II).

The second new effect (1.20) arises from $M_1' \, \alpha E$ interference (or $M_1' \, \beta E$ interference; see Eqs. B.9-10). It has all the characteristic features of the PV signal $\mathcal{F}^{pv}$ (Eq. 1.15) *except* its behaviour under reversal of the propagation direction $\hat{\mathbf{k}}$: $\mathcal{F}^{(1)}_{hf}$ is odd while $\mathcal{F}^{pv}$ is even. It is thus suppressed in the multipass (just like $\mathcal{F}^{(1)}$). The magnitude of the ratio $\mathcal{F}^{pv}/\mathcal{F}^{(1)}_{hf}$ is :

$$\sim (\hbar\omega^*_{hf}/\mu_B H)(\mathrm{Im}\, E_1^{pv}/M_1) \sim 10^{-1}/H_{Gauss} \quad \text{if} \quad \Delta F = 0,$$

$$\sim (\hbar\omega^*_{hf}/\mu_B H)(\mathrm{Im}\, E_1^{pv}/M_1')(\beta/\alpha) \sim 10^{-2}/H_{Gauss} \quad \text{if} \quad \Delta F = \pm 1,$$

for a *single* pass of the laser beam, and typically 2 or 3 orders of magnitude larger in the multipass configuration.

(ii) Hf mixing induces also new *ξ-independent* terms in the polarized fluorescence signal (Eqs. (B.4 to 7)). They are even under reversal of **E**. These characteristics, together with their weak magnitude in the compensated earth field, make them harmless as regards systematic effects in PV measurements. On the other hand their well defined signature and their size in a large known magnetic field make them interesting as reliable standards to calibrate the PV measurements. We discuss this point below.

1.3.2 *Hanle effect(s) and calibration of the electronic polarizations.* — In a magnetic field the second type of effect important here is the Hanle effect, which changes the direction of the stationary polarization. Possible Hanle effect in stray magnetic fields is included in our model of systematics (part II). On the other hand, by simply applying a field without any other change of the set-up, new polarized fluorescence signals can be detected.

(i) For example when **H** is along $\hat{\mathbf{k}} \times \hat{\mathbf{k}}_f$, the $\mathbf{P}^{(2)}$ component created along $\hat{\mathbf{k}}$ gives a known H-odd signal (cf. App. B, Eq. (B.13)). Since it is large in $\Delta F = 0$ components we use it as a standard to calibrate $\mathcal{F}^{pv}$. The calibration signal is then detected using the same optics and the same electronics as the PV signal (§ 2.10). Besides, noting that the relevant dimensionless function of H has a flat maximum (cf. App. B, Eq. (B.11)), one sees that the procedure does not even require the knowledge of the absolute magnitude of the magnetic field.

Yet since $\mathbf{P}^{(2)}$ is created in a direction normal to $\mathbf{P}^{pv}$, for the calibration method to be valid, the relaxation has to be isotropic in our geometrical configuration (despite the favoured directions of the electric field and of the laser beam, which selects atoms of

zero velocity-component along $\hat{\mathbf{k}}$). Several tests have been performed to check this isotropy [30]. But the most interesting of these tests does more : it checks the calibration method, in a direct manner, irrespective of any relaxation model. This test makes use of the spin polarization $\mathbf{P}_{hf}$ induced along $\hat{\mathbf{k}}_f // \mathbf{P}^{pv}$ by hf mixing in a known magnetic field $\mathbf{H} // \hat{\mathbf{k}}_f$. The value of $\mathbf{P}_{hf}$ is accurately predicted in a $\Delta F = 0$ component (Eq. (B.4)). The experimental value obtained by measuring $\mathbf{P}_{hf}$ and calibrating it with $\mathbf{P}^{(2)}$ as described above, is in good agreement with the prediction. Although $\mathbf{P}_{hf}$ could have been chosen in place of $\mathbf{P}^{(2)}$ to calibrate the parity experiment, $\mathbf{P}^{(2)}$ appeared more judicious for several reasons : i) it is larger by one order of magnitude for realistic field values; ii) it is independent of the calibration of the field $\mathbf{H}$; iii) it has the same dependence on the incident light polarization as $\mathbf{P}^{pv}$.

(ii) A second interesting configuration is obtained with $\mathbf{H}$ along $\hat{\mathbf{k}}$. It allows detection of the second component of $\mathbf{P}^{(2)}$ created along $\mathbf{E}$ when $\mathbf{E}.\hat{\mathbf{k}}$ is non zero (Eqs. (1.16) and (B.13)). This configuration thus proves useful for controlling imperfections of the direction of $\mathbf{E}$ (part II). In each configuration including a magnetic field, both hf mixing and Hanle effect are simultaneously present. Great care must be exercised to interpret the rich variety of new signals. However, as evidenced in table V, each signal has a definite dependence on the experimental parameters ($\mathbf{E}$, $\mathbf{H}$, circular or linear polarization of the incident light). In addition each signal undergoes definite sign and size changes when passing from one hfs component to another.

2. The experimental method and the apparatus.

In this section we describe the apparatus used to measure the PV amplitude, and the operating conditions.

The apparatus is shown schematically in figure 4. The cw laser beam passes through a polarization modulator, then undergoes in the caesium cell a multipass through the vapour. The polarization modulator and the multipass cell with internal mirrors both play an essential rôle in the experiment since they perform the reversals of ξ and $\hat{\mathbf{k}}$. These two key-elements have been designed and developed especially for this experiment. The polarization of the fluorescence light is analysed by a modulated circular analyser. The detection optics aims at high spectral selectivity and clean polarization analysis without excessive loss in collection efficiency. A detector of very low intrinsic noise has been selected. The modulations in the photocurrent are analysed at various combinations of the frequencies characteristic of the incident and detected polarizations, and the amplitudes are integrated. Various electric and magnetic field configurations can be arranged. During data acquisition a programmable calculator (HP 9825) assigns and controls all important parameters of the experiment.

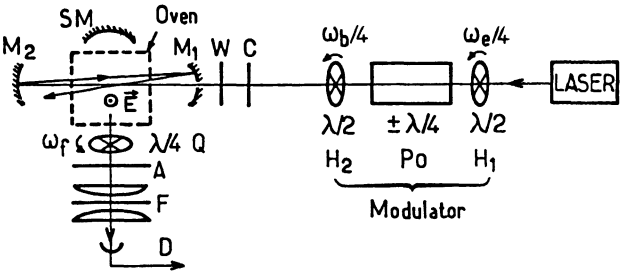

Fig. 4. — Apparatus. H_1, H_2 : rotating half-wave plates. Po : Pockels cell. C : birefringence compensator. W : entrance window. M_1, M_2 : multipass mirrors. SM : spherical mirror. Q : rotating quarter-wave plate. A : polaroid analyser. F : interference filter. D : detector.

Hereafter we review all important elements. In designing them we have paid considerable attention to reducing all potential sources of systematics. Our main goal was to reduce each possible systematic effect below a few percent of the expected PV asymmetry, so as to avoid the need for corrections. A second major concern was to minimize the noise and to increase the statistics. Towards the end of this section we discuss the important problem of signal/noise optimization which strongly influences the final choice of operating conditions.

2.1 THE LASER SOURCE. — The tunable ring laser (Spectra Physics 380) is pumped by the 5 145 Å line of a cw Ar^+ laser. The dye (Rhodamine 110 dissolved in ethylen glycol with pH = 7 ([4])) is cooled to about 12 °C. Steady output power of 500-600 mW is thus obtained in continuous single-mode operation for about 70 hours without changing the dye, but progressively increasing the pump power from 4 to 8 watts. We have observed that the need for frequent cavity readjustments mainly originates in dust deposition on the optics. We prevent this by continuously blowing into the cavity a gentle current of air passed through active carbon, then through pores of 0.25 μ diameter.

Frequency stabilization involves locking the intracavity etalon to the laser mode, which is in turn locked (through a galvoplate) to an external Fabry-Perot cavity tuned by air pressure to the atomic line. Typical jitter of a few MHz in the 0-1 kHz frequency band results in negligible noise in signal amplitude since the frequency is tuned to the peak of a broad line (Doppler FWHM ~ 750 MHz). Every time the correction voltage in either servo-loop drifts beyond

([4]) The normally acidic pH of the dye-glycol solution is increased to ≈ 7 by adding to 1.2 l of the usual solution, 4 cc of a water solution containing 180 g/l of K_2CO_3. We are indebted to Michael Dulick for indicating pH influence for Rhodamine 110 at 540 nm.

some threshold, an auxiliary correction voltage is readjusted so as to zero the error signal (« automatic recentring » [39]). In case of a sudden perturbation (e.g. a bubble in the jet), a « blanking » system shorts the integrator's capacitor in the galvo-loop until the error signal comes back to a reasonable value. Correct centring, maintained so far by the automatic recentring, guarantees that the loop locks again on the same mode in most cases. A lock-in detection time constant of 1.5 s is enough for the etalon loop not to become aware of anything. With this system, stable single-mode operation for 10 or 20 hours is commonplace. Unrecovered mode-hops are detected by the electronic « supervisor » which controls the locked status of most servo-loops. Data acquisition stops and manual readjustment of the laser is requested.

External intensity stabilization is ensured by a fast « light tap ». This consists of a Pockels cell (Lasermetrics 3079 FW) driven by fast amplifiers (1 GHz bandwidth) and followed by a Glan prism ([5]). The rms amplitude of the fluctuations between 0 and 1 kHz is reduced by a factor 500-1 000. The locked status of this loop too is controlled by the electronic supervisor. This loop is simultaneously used to apply a slight intensity modulation (typical depth 10^{-3}), generated by a second servo-loop, for fine compensation of a systematic effect (cf. §§ 2.3.5 and 2.4).

2.2 THE POLARIZATION MODULATOR. — Reversing the circular polarization is one of the means of interchanging the right and the left in the experimental configuration. The other parameters of the beam (intensity, linear polarization) should remain unchanged in this reversal. A change as small as 10^{-2} can be sufficient to generate a systematic effect of the size of the parity-violating effect. Four commercial modulators that we tried exhibited such imperfections at the level of several per cent. This led us to design a new system [40] where these imperfections are reduced to less than 10^{-4}.

2.2.1 *Principle.* — The polarization modulator (Fig. 4) consists of a Pockels cell, operated at $\pm \lambda/4$ voltage, sandwiched between two $\lambda/2$ plates rotating at different frequencies hereafter noted $\omega_e/4$ (input plate) and $\omega_b/4$ (output plate). The incident beam is polarized linearly. The polarization at the output is the superposition of a circular polarization and of a linear polarization whose direction rotates at frequency ω_b. Both are amplitude modulated at frequency ω_e but $\pi/2$ out of phase, so that the beam always remains fully polarized (see Fig. 5). The beam intensity is not modulated.

A general representation of the beam polarization properties is given by the Stokes parameters :

$$\begin{cases} u_0 = |\,\varepsilon_x\,|^2 + |\,\varepsilon_y\,|^2\,, \\ u_1 = 2\,\mathrm{Re}\,(\varepsilon_x^* \cdot \varepsilon_y)\,, \\ u_2 = 2\,\mathrm{Im}\,(\varepsilon_x^* \cdot \varepsilon_y)\,, \\ u_3 = |\,\varepsilon_x\,|^2 - |\,\varepsilon_y\,|^2\,, \end{cases} \tag{2.1}$$

where x and y are coordinate axes orthogonal to the propagation direction (z axis). The four Stokes parameters turn out to be the most directly measurable polarization parameters : u_0 is the « unpolarized intensity » of the beam, i.e. the intensity measured by receiving the beam on some detector. u_3 is the « xy-linearly polarized intensity », i.e. the difference between the intensities transmitted by a linear analyser directed along x then along y. In a similar way u_1 is the « bb'-linearly polarized intensity », where b and b' denote the bisectrices of the x and y axes; finally u_2 is the « circularly polarized intensity », i.e. the difference between the intensities transmitted by a direct and an inverse circular analyser.

At the output of the modulator each of these four parameters is labelled with a specific modulation. Normalizing $|\,\varepsilon\,|^2$ to unity and introducing the Pockels cell retardation δ, we obtain :

$$\begin{cases} u_0 = 1\,, \\ u_1 = \dfrac{1 + \cos\delta}{2} \sin(\omega_b - \omega_e)\,t - \dfrac{1 - \cos\delta}{2} \sin(\omega_b + \omega_e)\,t\,, \\ u_2 = -\sin\delta \cos\omega_e\,t\,, \\ u_3 = \dfrac{1 + \cos\delta}{2} \cos(\omega_b - \omega_e)\,t - \dfrac{1 - \cos\delta}{2} \cos(\omega_b + \omega_e)\,t\,. \end{cases} \tag{2.2}$$

In principle the voltage on the Pockels cell is adjusted so that $|\,\delta\,| = \pi/2$. Thus :

$$\begin{cases} u_0 = 1\,, & \text{(a)} \\ u_1 = \tfrac{1}{2}[\sin(\omega_b - \omega_e)\,t - \sin(\omega_b + \omega_b)\,t]\,, & \text{(b)} \\ u_2 = \eta' \cos\omega_e\,t\,, \quad \text{with} \quad \eta' = -\sin\delta = \pm 1\,, & \text{(c)} \\ u_3 = \tfrac{1}{2}[\cos(\omega_b - \omega_e)\,t - \cos(\omega_b + \omega_e)\,t]\,. & \text{(d)} \end{cases} \tag{2.3}$$

([5]) We are grateful to A. Brillet for giving us the schemes of this stabilization.

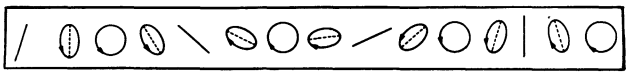

Fig. 5. — The beam polarization at the output of the polarization modulator, represented at equal time intervals ($t = \pi/4\,\omega_e$).

2.2.2 *Experimental implications.* — We have verified experimentally that the amplitude of the modulation in principle specific of a given Stokes parameter u_k, but spuriously present in an other parameter $u_{l\neq k}$, actually remains very small. In particular, the amplitude of the spurious $\eta' \cos \omega_e t$ modulation in u_0, u_1 or u_3 remains $< 10^{-4}$. Thus each modulation (including the behaviour under η' reversal) is to a high degree a *specific* signature of the corresponding u_k. The low values of the spurious cross-modulations originate in the *double* distinction established between any two Stokes parameters by the very design of the modulator [40]. As a result, spurious cross-modulations are *second-order* effects involving the product of two small imperfections (such as etalon effects in the rotating plates or in the Pockels cell; transmission or retardation inhomogeneities in the rotating plates; retardations not exactly half-wave; ...).

In our experiment the axes of the Pockels cell are oriented at $\pm$ 45° with respect to the applied electric field **E**. (This orientation provides a convenient method to align the Pockels cell and to adjust its voltage for $|\delta| = \pi/2$ using atomic signals; § 2.2.3). We choose the y axis (involved in (2.1)) along **E**. Then in the ideal configuration (Sect. 1, Fig. 3), x is along the detection direction (Fig. 6). The four Stokes parameters are then inserted in the expressions of the fluorescence signals (Table V). The photon helicity ξ involved in $\mathcal{F}^{pv}$, $\mathcal{F}^{(2)}$ and $\mathcal{F}^{(0)}$, is given by :

$$\xi = u_2/u_0 = \eta' \cos \omega_e t\,. \tag{2.4}$$

The ξ-independent signals involve the three other Stokes parameters u_0, u_1, u_3, according to :

$$\left.\begin{aligned} 2\,|\,\hat{\mathbf{E}}\cdot\boldsymbol{\varepsilon}\,|^2 &= u_0 - u_3 \\ 2\,|\,\hat{\mathbf{E}}\times\boldsymbol{\varepsilon}\,|^2 &= u_0 + u_3 \end{aligned}\right\} \tag{2.5a}$$

$$\left.\begin{aligned} 2\,\mathrm{Re}\,[(\boldsymbol{\varepsilon}\cdot\hat{\mathbf{E}})(\boldsymbol{\varepsilon}^*\times\hat{\mathbf{k}})] &= (u_0 - u_3)\,\hat{\mathbf{x}} - u_1\,\hat{\mathbf{y}} \\ 2\,\mathrm{Re}\,[(\hat{\mathbf{k}}\times\boldsymbol{\varepsilon}\cdot\hat{\mathbf{E}})\,\boldsymbol{\varepsilon}^*] &= (u_0 + u_3)\,\hat{\mathbf{x}} + u_1\,\hat{\mathbf{y}} \end{aligned}\right\} \tag{2.5b}$$

$$2\,\mathrm{Re}\,[(\hat{\mathbf{E}}\cdot\boldsymbol{\varepsilon})(\hat{\mathbf{E}}\times\boldsymbol{\varepsilon}^*)] = -u_1\,\hat{\mathbf{z}} \tag{2.5c}$$

($\hat{\mathbf{E}}$ is a unit vector along **E**).

2.2.3 *Practical realization; adjustments.* — In practice the components of our modulator are a longitudinal-field Pockels cell (Lasermetrics 1057 FW) and two 3 $\lambda/2$ quartz plates. The plates are mounted in two rotors suspended and driven into rotation by compressed air ($(1/2\pi)(\omega_e/4) = 115.2$ Hz; $(1/2\pi)(\omega_b/4) = 85.65$ Hz). To generate reference waveforms for the lock-in detectors, alternated black and white 45° sectors are painted on the rotors. Light from a small lamp, illuminating them through one leg of a V-shaped optical fibre, is scattered through the second leg to a photodiode. Pressure reducer-stabilizers (SEIEM Nullmatic 40-15) are used on the air inlets.

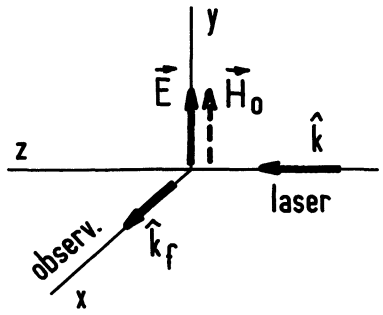

Fig. 6. — Definition of the coordinate axes.

In the PV experiment the choice of the frequencies is not arbitrary (§ 2.9.2) and should be subsequently abided by. Therefore the rotation frequencies are stabilized (to $\sim$ 1 part in 10^3) by repeated digital measurement and correction through a micromotor driving the pressure reducer.

The Pockels cell incidence is initially aligned for zero retardation at zero voltage. Zero retardation is achieved when only one modulation frequency ($\omega_b - \omega_e$) is observed in the linearly polarized intensities u_1 or u_3 (cf. Eqs. (2.2) with $\delta = 0$), analysed using a prism or *via* the atomic signal $\mathcal{F}_u$ (Eqs. (1.12) and (2.5a)). During data acquisition we repeatedly check the conservation of the fluorescence intensity $\mathcal{F}_u$, i.e. of $|\delta|$ under reversal of the Pockels cell voltage. If necessary a small bias v is applied, i.e. the voltage is switched between $-V + v$ and $+V + v$. In practice v/V never exceeds 10^{-3} and the asymmetry in $\mathcal{F}_u$ when δ is reversed remains below noise.

To adjust the voltage V for quaterwave retardation we remove the output $\lambda/2$ plate. The output polarization becomes $u_1 = \sin \omega_e t$; $u_2 = \sin \delta \cos \omega_e t$; $u_3 = \cos \delta \cos \omega_e t$. The atomic signal $\mathcal{F}_u$ then exhibits (through u_3) a modulation at frequency ω_e, whose amplitude vanishes for $|\delta| = \pi/2$. Given the stability of the room temperature ($\Delta\theta < 0.5$ °C), thermal stabilization of the Pockels cell has not been necessary. To reverse the Pockels cell voltage, the order ($+-$ or $-+$) of each new pair of signs is electronically drawn by lots.

2.3 THE MULTIPASS CELL WITH INTERNAL MIRRORS. — In § 1.2.3 we explained the interest of a beam multipass configuration (handedness reversal + signal amplification). The very low absorption of the highly forbidden line (2×10^{-7} per pass in realistic conditions) allows the multipass to be very effective provided no losses (i.e. no windows) are introduced between the mirrors. These must therefore be located inside the caesium cell.

2.3.1 *Principle of a multipass cavity* [41]. — The Cs vapour is placed between two spherical mirrors facing one another. The laser beam enters through a small hole drilled at the centre of one mirror, and bounces from one to the other mirror (Fig. 7). For a discrete set of particular values of the mirror spacing, after some number of forward-backward passes, the beam comes back exactly to the entrance hole and escapes the cavity. (For other spacing values, one beam impact will overlap the entrance hole, causing the beam to be scattered or split in an uncontrolled way and making the multipass unusable). The direction of the emerging beam is symmetrical to that of the incident beam with respect to the cavity axis (line of the centres of curvature of the mirrors). The loci of the beam impacts on the mirrors are two ellipses (one on each mirror); their common size, shape and orientation can be chosen by adjusting the orientations of the mirrors and of the incident beam. The (always even) number of passes is chosen by adjusting the spacing.

In a first analysis the number $2N$ of passes and the reflectivity r of the mirrors determine the gain in fluorescence signal $\mathcal{F}_u$

$$G = 1 + r + \cdots + r^{2N-1} = (1 - r^{2N})/(1 - r),$$

as well as the reduction factor for the signal $\mathcal{F}^{(1)}$, odd under reversal of the beam direction :

$$R = 1 - r + \cdots - r^{2N-1} = (1 - r^{2N})/(1 + r).$$

Consequently the polarization ratio $\mathcal{F}^{(1)}/\mathcal{F}_u$ associated with $P^{(1)}$ is reduced by a factor $(1 - r)/(1 + r)$ involving only the reflectivity. Yet to explain all our observations we must account for slight geometrical effects : since the passes do not exactly coincide, they are not detected with exactly the same efficiency. Typical values are $2N = 120-130$, $1-r = 1 \times 10^{-3}$. We observe a gain $\sim$ 100 for $\mathcal{F}_u$. During Exp. 1 the observed reduction factor for $P^{(1)}$ was $\sim$ 180; during Exp. 2, $\sim$ 2 000.

The laser mode is matched to the cavity by a lens. In order to reduce the height of the observation region (for more effective light collection, and also for reasons connected with stray birefringences; § 2.3.5), we choose very flat ellipses (long axis $\approx$ 23 mm, horizontal; short axis $\approx$ 2 mm, vertical $/\!/\mathbf{E}$). A diaphragm (∅ 1 mm) fixed 1 m before the entrance hole (∅ 1 mm) allows the beam position to be quickly restored (within 1 mrad) after readjustment of the laser cavity.

2.3.2 *Design of the cell.* — Caesium vapour at 200 °C is fatal to multidielectric mirrors. Our solution to this problem, explained in detail in reference [42], is schematized in figure 8. The cell basically consists of a long glass tube with a stainless steel assembly supporting one mirror at each end. The hot caesium vapour is confined in the centre part, while the mirrors are in the cooled ends.

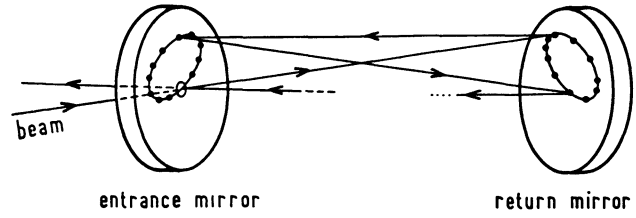

Fig. 7. — The multipass. Not all passes are represented. For clarity the angles between passes (actually $\sim 1 \times 10^{-2}$ rad) are considerably exaggerated.

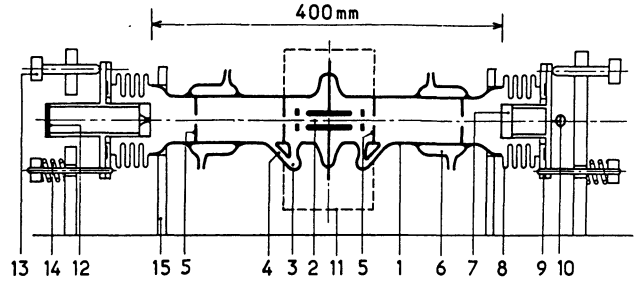

Fig. 8. — Overall scheme of the multipass caesium cell (1 : glass tube; 2 : observation region with electric field plates; 3 : caesium reservoirs; 4 : return tubes; 5 : diaphragms; 6 : water coolings; 7 : mirrors; 8 : bellows; 9 : flanges with copper gaskets; 10 : repumping valve; 11 : oven; 12 : entrance window; 13 : mirror adjustment screws; 14 : springs; 15 : stand).

The centre part includes the observation region, filled with Cs vapour at 185-200 °C and provided with electrodes (§ 2.3.4), and the reservoirs of liquid caesium. A buffer gas (helium; $p \sim$ 0.15-0.35 torr) and diaphragms (cut so as to allow the beam multipass) limit the outward flux of Cs vapour ([6]). In the tepid region between the hot centre and the water coolings (12 °C), caesium escaped through the diaphragms condenses as liquid droplets, which end in streaming back by gravity to the reservoirs through narrow slant tubes. Caesium stuck in the solid state near the water coolings is recycled by melting with a hair-drier (typically every 70 hours of operation) while data acquisition is stopped. The caesium pressure is fairly stable, except very slow drifts between the saturation value and roughly two thirds of it. The mirrors turn out to be sufficiently protected to avoid loss of reflection for the duration of a complete run (several weeks).

The mirror assemblies include bellows for adjustability. The mirror spacing is nearly equal to their curvature (R = 400 mm). All materials (747 glass; 18/10 stainless steel; tungsten rods with oxideless feedthroughs for the electrode rods) are insensitive to caesium.

([6]) The second pair of diaphragms, placed inside the water coolings (Fig. 8), was added for Exp. 2 performed at lower He pressure.

The empty cell is first outgassed by pumping at 300 °C for several days. Then 15 g of caesium are added and the mirrors and window are mounted under helium atmosphere (O_2 and H_2O concentration < 1 ppm) inside a glove-box.

2.3.3 *Oven.* — Because of the infrared detection wavelength (1.36 μ) thermal radiation from the oven (at 200 °C) cannot be neglected even though an interference filter is interposed. In designing the oven we have tried to : i) optimize thermal contact between the cell and the heating elements, so as to reduce the temperature and radiation of the latter; ii) reduce the absorptive power, i.e. the emissive power with respect to blackbody radiation.

In our two-level oven, the lower compartment containing the Cs reserve is heated ≈ 15 °C less than the upper part containing the cell body, so as to protect the transparent wall of the cell from being dimmed by caesium condensation. Some insulation between top and bottom is obtained with quartz wool and aluminium foil. The two temperatures are stabilized independently. In the lower part, thermal contact between heaters and glassware is ensured by small shot; in the upper part, by a block of brass machined so as to fit the glass body of the cell, and wrapped in aluminium foil to reduce its absorptive power. The heaters are outside the field of view of the detector. The oven windows, 10 mm thick Infrasil discs, are antireflection coated. To avoid stray magnetic fields we heat with 2-conductor thermocoax.

2.3.4 *Electrodes, diaphragms and potential map.*

2.3.4.1 Electrode and diaphragm configuration. — Figure 9 shows the electrodes and diaphragms. The plane capacitor produces the dc field for the electroweak interference. The ring-shaped auxiliary electrodes, in principle unused during PV measurements, are designed so as not to perturb the field inside the plane capacitor. They are used to produce a small field component along the cell axis for auxiliary measurements, or to compensate possible stray fields.

The main electrodes, 10 mm apart, are thick rectangular plates (33 × 23 × 3 mm³) with edges cut to a half-circle profile. The auxiliary electrodes, 1 mm thick and 48 mm apart, are ring-shaped to allow the beam multipass. A flat spring collar soldered in one point surrounds each diaphragm and holds it in position. Except the tungsten rods, all parts are made of stainless steel and heated to 1 000 °C under hydrogen atmosphere before being assembled.

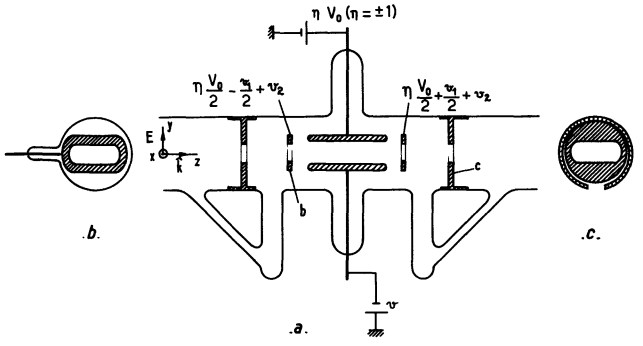

Fig. 9. — a) Electrode and diaphragm configuration with potentials (hatches : stainless steel; capacitor rods : tungsten ; other : 747 glass) ; b) auxiliary electrode ; c) diaphragm with spring collar.

We have found that a laser spot on an electrode can start a discharge in conditions otherwise satisfactory. Protection of the electrodes from stray (reflected or scattered) laser light is also an essential rôle of the diaphragms.

2.3.4.2 Voltages. — The voltage configuration during PV measurements is also shown in figure 9. ηV_0 ($\eta = \pm 1$) is the periodically reversed high voltage (typical values 120 V and 650 V during Exp. 1 and Exp. 2 respectively). $v \ll V_0$ is a small correcting bias assigned by the program so that the unpolarized fluorescence signal $\mathcal{F}_u \propto E^2$ remains the same for both signs of the high voltage. The auxiliary electrodes should in principle be held at a common voltage close to $\eta V_0/2$. This minimizes the distortion of the field lines at their intersection with the symmetry plane (xz plane) which precisely contains the beam multipass, carefully centred at half-distance between the plates. In fact, a small voltage v_1 can be applied across the auxiliary electrodes to compensate a possible stray field along z (< 40 mV/cm). In addition, because the auxiliary electrodes are in practice slightly asymmetric with respect to the yz plane, application of a (small) *common* unreversed voltage v_2 allows compensation of a stray field component along x (< 25 mV/cm). Stray fields are measured using atomic signals (part II).

To avoid accidental correlations with linear or periodic drifts, in reversing η the order (+ − or − +) of every new pair of signs is chosen at random. To avoid causal correlations, the voltage is reversed by use of two relays in series : one is reversed in a fixed + − order while the other is reversed following the random sign pair method.

An axial electric field proves useful to control imperfections of the main field **E** and of its reversal (part II). For these controls, performed during auxiliary measurement sequences, large opposite voltages + $V_e/2$ and − $V_e/2$ are applied to the auxiliary electrodes. By symmetry, the transverse field component remains in principle unchanged on the average in the (correctly centred) observation volume. In practice we have to allow for the small dissymmetry in the electrodes, resulting in a small uncertainty in the control method.

2.3.4.3 Electric field map. — Due to the finite size of the plane capacitor and to the vicinity of other conductors, the main field is not rigorously uniform in magnitude or direction. We have studied this numerically by finite difference resolution of the Laplace equation.

Inhomogeneities in the magnitude of the electric field affect the calibration of the PV experiment. One important parameter is the average value of the component E_y normal to the plates, taken over the observation volume. Our result is :

$$\langle E_y \rangle = k \times (1 + 2.8 \times 10^{-2}\, y_{mm}) \times V_0/d. \quad (2.6)$$

Here d is the electrode spacing; y is the average height above the symmetry plane (in principle zero). This symmetry-beaking y-term originates in grounded conductors (oven, glass wall with Cs film) surrounding the observation region. The coefficient k depends on the dimensions of the observation region. For dimensions (in mm) $8 \times 1 \times 5$ along x, y, z (case of Exp. 1) we find $k = 0.987$; for $8 \times 1 \times 12$ (Exp. 2), $k = 0.982$. The plate parallelism is correct within a few 10^{-3} rad. Uncertainties in d (0.5 %), in y and in the numerical model result in ~ 1 % uncertainty in $\langle E_y \rangle$. The calculation also shows that $|\partial E_y/\partial y| > |\partial E_y/\partial x|$. This is one more reason to squeeze the y-dimension of the multipass.

Tilts resulting from edge effects vanish in the average over the observation region. However their rms values amount to 9×10^{-2} along x, and 0.6×10^{-2} or 1.7×10^{-2} along z (for a length of 5 or 12 mm resp.). As expected the tilt along z is sensitive to the common potential applied to the auxiliary electrodes; the above values correspond to the practical case where this potential is close to $\eta V_0/2$. Atomic signals (part II) yield experimental values of these tilts (not only average values, but also dispersions and gradients, by varying the observation volume). The numerical results and the atomic results agree.

Since the auxiliary electrodes are designed so as not to perturb the main field, inside the plane capacitor their (axial) field is screened, i.e. both attenuated and inhomogeneous. The average value e for a voltage V_e is a function of the length l of the observed region. It is measured to be :

$$e/V_e\,(\mathrm{cm}^{-1}) \approx 1.5 \times 10^{-2} \quad \text{for} \quad l \approx 9\ \text{mm} \quad \text{(Exp. 1)},$$
$$3 \times 10^{-2} \quad \text{for} \quad l \approx 25\ \text{mm} \quad \text{(Exp. 2)},$$

in agreement with the numerical estimation.

2.3.5 *Birefringences in the caesium cell.* — Birefringence and circular dichroism, which transform helicity (i.e. handedness) reversal into modification of the linear polarization or intensity of the light, are potential sources of systematic effects in the PV experiment. The theoretical analysis [43, 44] is developed in part II. Among the two components of the birefringence, the component whose axes lie at $\pm$ 45° with respect to the electric field **E** turns out to be much more harmful. A few experimental details are collected below.

Circular dichroism in our optics was measured to be negligible (less than 10^{-6}), therefore only birefringence has to be considered. Birefringence in the caesium cell has three physical origins : birefringence in the window; birefringence from phase-shifts in the reflections under non-zero incidence on the mirrors; birefringence from anisotropy in the mirror coatings. We choose a window of low birefringence (Hellma, 1.25 mm thick Suprasil, biref. $\lesssim 10^{-3}$ rad) and stick it on the polished stainless steel extremity of the cell using flexible adhesive (Eccobond 45, flexible formulation). Nevertheless stress from pressure difference (1 at. outside, less than 1 torr inside) results in birefringence $\sim 5 \times 10^{-3}$ rad.

To reduce the consequences of off-normal-incidence birefringence (typically 1.3×10^{-5} rad per reflection in our case) we orientate one of its average axes along the electric field **E**. Since by symmetry the average birefringence axes are the ellipse axes, we simply adjust one of these (the short axis) to lie along **E**. (This adjustment is realized by means of cathetometer aimings. We bring both the capacitor plates and the long axis to be horizontal). In practice, because different passes in the multipass may be viewed by the detector with slightly different efficiencies, this symmetry argument is not strictly valid. Therefore, as an extra precaution we nearly degenerate the ellipse into its long axis. Then for most reflections one of the local birefringence axes lies nearly along **E**.

Birefringence in the mirror coatings, studied in great detail [44], is typically 10^{-4} rad, but only our best mirrors (10^{-5}-10^{-6} rad) were retained for the PV measurements. The coating birefringence is essentially uniform, so that the principal axes can be determined and oriented parallel and normal to the electric field to minimize the effects.

The above precautions are taken when the cell is being assembled or installed, i.e. *previous to* the PV measurements, to *reduce the sources* of trouble. A second class of steps are taken in real time, i.e. *during* (or immediately before) the PV measurements, to *compensate* the residual trouble. The overall birefringence of the entrance window and of the multipass, which magnitude and axes are known and cross-checked from several atomic signals (part II), is compensated with a Babinet-Soleil-Bravais compensator (birefringence variation per unit displacement 8×10^{-3} rad/mm) placed before the window. Because thermal gradients have been observed to induce birefringence drifts, the compensator and the window are each shielded by a dural box with external felt lining. In principle, adjusting both the orientation and thickness of the compensator allows simultaneous compensation of both parameters of the birefringence. In practice, inhomogeneities in the compensator or slightly off-normal incidence cause slight retardation changes ($\sim 10^{-3}$ rad) when the orientation is rotated. Therefore whe have compensated in priority, to within $\sim 10^{-3}$ rad, the more harmful component, i.e. the one with axes at $\pm$ 45° of the electric field. The less harmful one is compensated to within $\sim 2 \times 10^{-3}$ rad. Further compensation of the effect of the worse com-

ponent (to within 8×10^{-5} rad) is achieved by opposing an artificial circular dichroism, realized as a slight modulation ($\approx 10^{-3}$) of the laser intensity with the frequency and phase of the helicity (§ 2.4 and part II).

As explained in reference [43] and part II, birefringence in the return mirror is particularly dangerous. Although its axes are initially oriented so as to minimize its effect, evolution (over a few months) is sometimes observed. As a protection, in Exp. 2 the return mirror was mounted on a vacuum-tight rotatory feedthrough (Ferrofluidics), and a $\pi/2$ rotation was performed once every 24 hours. The systematic effect ($< 10\,\%$ of the PV effect in the worst case, i.e. for 45° spontaneous rotation of the axes) is then reversed, so that the averaged effect is brought down below the percent level. In Exp. 1 the mirror rotation was not yet installed. However the return mirror birefringence was checked before and after the measurements. Its value was low ($\sim 3 \times 10^{-6}$ rad) and no troublesome evolution was observed.

2.4 FINE COMPENSATION OF THE SYSTEMATIC EFFECT OF BIREFRINGENCE BY MODULATION OF THE LASER INTENSITY. — At this point the more harmful component of the residual overall birefringence is typically 10^{-3} rad. We now describe a method to further reduce its effect by one order of magnitude.

2.4.1 *Principle.* — Birefringence introduces the signature of the helicity ξ into Stokes parameter u_3, and consequently into $\mathcal{F}^{(1)}$ (systematic effect) and into $\mathcal{F}_u$ (cf. Eqs. (2.5)). The spurious (i.e. ξ-like) modulation in $\mathcal{F}^{(1)}$ can be compensated by means of a slight modulation of same frequency and opposite phase in the laser intensity. The amplitude of this modulation is conveniently adjusted by monitoring its effect in $\mathcal{F}_u$. A detailed analysis (part II) shows that the spurious modulation in $\mathcal{F}_u$ should not be exactly compensated to zero, but to some known fraction κ of its free value. (For the determination of κ see part II, appendix E).

Spurious modulation $\pi/2$ out-of-phase with ξ has at first sight no effect on the parity signal. Yet as described below (§ 2.9.1) the parity signal is detected in phase with the product $\xi\xi_f$ of 2 modulations characteristic of ξ and of the detected helicity ξ_f respectively. Therefore spurious modulation $\pi/2$ out-of-phase with ξ might generate problems in the parity channels by combining with spurious modulation $\pi/2$ out-of-phase with ξ_f (due to imperfections in the circular analyser). In addition we want to check the absence of signal $\pi/2$ out-of-phase with the parity signal (part III). Therefore we have decided to cancel also the spurious modulation $\pi/2$ out-of-phase with ξ (typical depth $< 10^{-3}$) observed in $\mathcal{F}_u$.

2.4.2 *Realization.* — The desired modulation is applied to the reference voltage V_{ref} of the laser intensity stabilization (Fig. 10a). To prepare it, two reference sinewaves, one in-phase and one $\pi/2$ out-of-phase with the helicity ξ, are generated from the reference

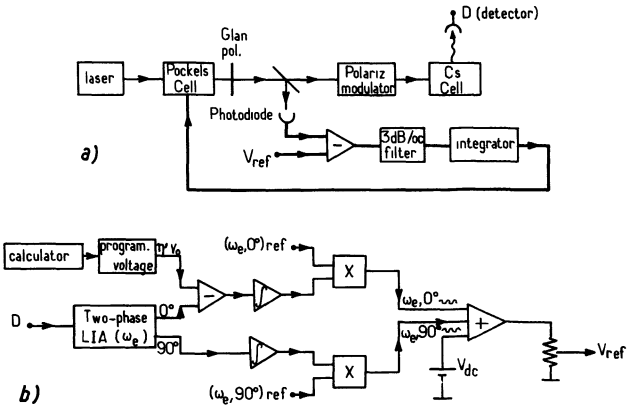

Fig. 10. — a) Laser intensity stabilization servo-loop; b) generation of the intensity reference.

signal at frequency ω_e (cf. § 2.2.3). Using these reference waveforms, a two-phase lock-in amplifier extracts the amplitudes of the corresponding modulations observed in the unpolarized fluorescence signal $\mathcal{F}_u$ (Fig. 10b). After integration (for high dc loop-gain) the *out-of-phase* amplitude is multiplied by the out-of-phase reference sinewave (of fixed amplitude) to produce the out-of-phase correcting modulation. The in-phase channel is similar, except an offset voltage under program control. This voltage allows for the offset parameter κ mentioned in § 2.4.1. It is reversed with η' (the sign of the $\lambda/4$ voltage in the polarization modulator), so as to exhibit the signature of the helicity (Eq. (2.4)). The two (small) correcting modulations thus generated are then added to the (large) dc voltage that defines the dc level of the stabilized intensity. (In spite of this superposition, the in-phase and out-of-phase channels are independent, because of their $\pi/2$ phase difference).

The modulation at frequency ω_e in the laser intensity mixes with the large modulations at frequencies $\omega_e \pm \omega_b$ in $\mathcal{F}_u$ and generates modulations at frequencies $\omega_e \pm (\omega_e \pm \omega_b)$. By lock-in detection at frequency $2\,\omega_e - \omega_b$ we control the operation of the system, and also obtain a real-time value of the birefringence effect being compensated. The result cross-checks the birefringence value measured in open servo-loop without laser intensity modulation, during auxiliary sequences (part II).

2.5 MAGNETIC FIELD. — Magnetic field components up to 20 G can be applied along x, y, or z (Fig. 6) by means of three pairs of coils. Auxiliary windings allow the compensation of stray fields whose magnitude is deduced from atomic signals (cf. part II). The coils are square (side length $a = 367$ mm). The y pair is at Helmholtz spacing ($S/a = 0.54$). For reasons of tabletop convenience the x and z pairs are not ($S/a \simeq 1.2$ and 1.6 respectively). Yet inhomogeneities in the observation region remain $< 3 \times 10^{-3}$. The windings are shorted with capacitors to avoid damage when the voltage is reversed.

During data acquisition we monitor the compensating current of the stray y component whose spurious variations correlated with E-reversal would be harmful in Exp. 1. For this a microvoltmeter measures the voltage across a stable (manganin) resistor in series with the coils. We also continuously monitor the fluctuations of the earth field using a fluxgate. The probe is located near the centre of the Cs cell, and oriented so as to probe the most harmful component (along y or z in Exp. 1 or 2 resp.; cf. part II).

2.6 DETECTION OPTICS. — The fluorescence beam and the detection optics are shown in figure 11. The $7S_{1/2}$-$6P_{1/2}$ fluorescence light ($\lambda = 1.36\ \mu$), passes through a circular polarization analyser, composed of a rotating quarterwave plate followed by a fixed linear analyser. The 3 $\lambda/4$ quartz plate (∅ 80 mm), adhered on a 10 mm thick Suprasil disc is suspended and driven into rotation by compressed air (rotation frequency $\omega_f/2 = 33.95$ Hz). The linear analyser is a Polaroid HR sheet (transmission for unpolarized light 0.36). The selected helicity is modulated :

$$\xi_f = \sin \omega_f t\,. \qquad (2.7)$$

The transmitted intensity contains a modulation at frequency ω_f, whose amplitude is proportional to the helicity of the emitted fluorescence. The polarized fluorescence signal is found to be discriminated against the unpolarized one at a level $< 10^{-3}$. The transmitted light is collected onto the detector by a doublet of planoconvex lenses (∅ 90 mm; $f = 130$ mm each; flint, $n = 1.767$; effective aperture deduced from atomic signals : $f/3$) operating close to unit magnification. Thermal radiation from the oven is rejected by an interference filter (∅ 80 mm; $\lambda_0 = 1.358\ \mu$; $\Delta\lambda = 45$ Å; transmission 0.61; effective index 1.45; Infrared Industries), backed by a blocking filter (peak transmission 0.66) placed just before the detector.

The detector (Applied Detector Corporation) is an intrinsic Ge photodiode operating at liquid N_2 temperature (quantum efficiency $\simeq 0.6$; NEP $\simeq 10^{-15}$ W/Hz$^{1/2}$), shielded with 12 mm thick lead against environmental radioactivity. Since the laser beam multipass is nearly degenerated into a flat ribbon which is viewed laterally from within its plane (Fig. 12), the sensitive area of the detector is chosen rectangular. Its height ($\simeq 6$ mm) allows for image broadening of the ribbon-shaped object (1-1.5 mm thick) due to field depth ($\simeq 16$ mm). Its length (9 mm in Exp. 1; 25 mm in Exp. 2) determines that of the observed region.

The light emitted in the $-x$ direction is reflected back in the $+x$ direction with 70 % efficiency by a spherical mirror (of curvature $R \simeq 70$ mm, equal to its distance from the cell axis). In spite of great care in optimizing all optical components, the detection efficiency is low : among all 1.36 μ photons emitted in the observed region only one in 700-1 000 reaches the detector. This estimation based on the measured individual transmissions of the optical components,

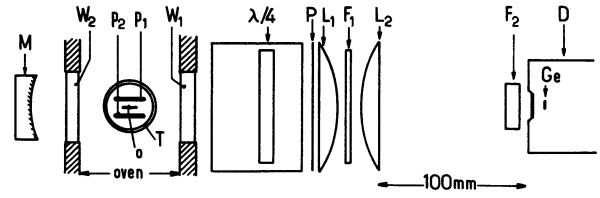

Fig. 11. — Detection optics; M : spherical mirror, O : observation region ; p_1, p_2 : capacitor plates ; T : glass tube of the caesium cell; W_1, W_2 : oven windows; $\lambda/4$: rotating $\lambda/4$ plate with acoustical insulation; P : Polaroid polarizer; L_1, L_2 : lenses; F_1 : interference filter; F_2 : blocking filter; D : nitrogen-cooled dewar; Ge : sensitive germanium area.

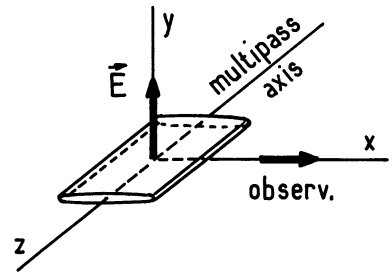

Fig. 12. — Limits of the observed interaction region : the bundle of beams actually envelopes the drawn volume.

agrees with the value deduced from the predicted and observed fluorescence yields (knowing the detector's responsivity). This low efficiency appears as the price paid for selective filtering and clean polarization analysis of the fluorescence light.

2.7 ORTHOGONALITY ADJUSTMENTS. — Imperfect orthogonality between the electric field direction $\hat{\mathbf{E}}$, the laser beam $\hat{\mathbf{k}}$ and the detection direction $\hat{\mathbf{k}}_f$ can combine with other imperfections to give rise to systematic effects (part II, §§ 3.3 and 3.4). Orthogonality of $\hat{\mathbf{E}}$ with both $\hat{\mathbf{k}}$ and $\hat{\mathbf{k}}_f$ is initially obtained to within 10^{-3} and 10^{-2} rad respectively, by adjusting the multipass axis (i.e. the line joining the centres of the two ellipses), the mechanical axis of the detection optics and the capacitor plates to be all horizontal. This is achieved by means of cathetometer aimings. Simultaneously, the multipass axis is set for equal distance from both capacitor plates, and the long axis of the ellipses is made horizontal (§ 2.3.5). Orthogonality of $\hat{\mathbf{k}}$ and $\hat{\mathbf{k}}_f$ is initially obtained by centring the ellipses on the mirrors and by accurate mechanical machining.

In a second step, atomic signals (§§ 3.3 and 3.4) are used to control the residual imperfections and reduce them further. Then the spherical mirror is installed and adjusted for $\hat{\mathbf{E}}\cdot\hat{\mathbf{k}}_f \sim 10^{-3}$ and $\hat{\mathbf{k}}\cdot\hat{\mathbf{k}}_f < 10^{-2}$ rad.

During data acquisition, fine readjustments (a few mrad) of $\hat{\mathbf{E}}\cdot\hat{\mathbf{k}}_f$ were sometimes necessary. In Exp. 1 ($\Delta F = 0$) we used Hanle effect in a magnetic field (~ 10 mG) along $\hat{\mathbf{k}}$: a rotation of the electronic polarization is equivalent to an opposite rotation of the

direction of observation $\hat{\mathbf{k}}_f$. In Exp. 2 ($\Delta F = 1$) this field would have been troublesome. We preferred a small readjustment of the return mirror of the multipass, so as to shift the observation region along x. Because of the slight inhomogeneity of the electric field, this results in a small change in its average direction $\hat{\mathbf{E}}$ (2 mrad for 0.1 mm).

2.8 SUMMARY ABOUT THE QUALITY OF THE PARAMETER REVERSALS. — We collect in table VI the figures concerning the quality of the main reversals involved in the expected systematic effects to be discussed later (part II).

2.9 SIGNAL PROCESSING.

2.9.1 *Principle.* — In the ideal configuration (and in absence of magnetic field) the polarized fluorescence signal reduces to the parity signal (§ 1.2.3)

$$\mathcal{F}_p = \mathcal{F}^{pv} \propto \eta(\delta_{FF'}\,\alpha + g_{FF'}\,\beta)\,E\,\mathrm{Im}\,E_1^{pv}\,\xi\xi_f\,.$$

The helicity ξ of the laser beam and the helicity ξ_f selected by the circular analyser are modulated (Eqs. (2.4) and (2.7)), resulting in a modulation in the photocurrent :

$$\xi\xi_f = \eta' \cos\omega_e t \sin\omega_f t = \frac{1}{2}\eta'[\sin(\omega_e + \omega_f)t - \sin(\omega_e - \omega_f)t]\,. \quad (2.8)$$

This modulation appears at frequencies $\omega_e \pm \omega_f$, with known phases. Its amplitude, proportional to $\eta\eta'\,\alpha E\,\mathrm{Im}\,E_1^{pv}$ or $\eta\eta'\beta E\,\mathrm{Im}\,E_1^{pv}$ in the $\Delta F = 0$ or $\Delta F = 1$ case respectively, is called the « PV amplitude ». It is odd under reversal of η (Stark voltage) or η' (Pockels voltage). We measure it by lock-in detection at both frequencies $\omega_e \pm \omega_f$ and extraction of the η-odd, η'-odd part (see § 2.10).

According to (1.12), (2.5a) and (2.3d), the unpolarized fluorescence signal $\mathcal{F}_u$ is modulated like

$$u_3 = \frac{1}{2}[\cos(\omega_e - \omega_b)t - \cos(\omega_e + \omega_b)t]\,,$$

at frequencies $\omega_e \pm \omega_b$. The modulation amplitude, proportional to $\alpha^2 E^2$ (for $\Delta F = 0$) or $\beta^2 E^2$ (for $\Delta F = 1$), is high above the noise. Therefore we measure it at only one frequency ($\omega_e + \omega_b$). We use it to normalize the PV amplitude. The « PV polarization ratio » thus built is insensitive to drifts in the vapour pressure as well as in the laser intensity or frequency.

2.9.2 *Contents of the photocurrent.* — At the output of the detector four types of signals have to be separated; these are :

i) The large modulations at frequencies $\omega_e + \omega_b$ and $\omega_e - \omega_b$ associated with the unpolarized fluorescence signal $\mathcal{F}_u$.

ii) Small modulations buried in the noise : the PV modulations at frequencies $\omega_e \pm \omega_f$; but also several modulations at various combinations of the basic frequencies ω_e, ω_b and ω_f, carrying information useful in estimating the importance of systematic effects (part II).

iii) Stray modulations at various combinations of harmonics of the rotation frequencies $\omega_e/4$, $\omega_b/4$ and $\omega_f/2$. They are associated with imperfections of the rotating plates. Their amplitudes can reach several percent. The presence of such a stray modulation within the bandwidth of the lock-in detection in a parity channel would be a source of extra noise and would require to reduce the sensitivity of this channel.

Table VI. — *Frequency and imperfections of the main reversals during Exp. 1 and Exp. 2.*

Reversed parameter	Repetition rate (or modulation frequency)	Imperfections: Nature	Typical size (measured from atomic signals): Exp. 1	Exp. 2
Beam direction (ξ & $\hat{\mathbf{k}}$)	∞ (both directions present)	residual fraction of $P^{(1)}$	5×10^{-3}	5×10^{-4}
Incident helicity ξ	460.8 Hz modulation + random phase reversal every 40 s.	spurious ξ-like modulation in u_1 in u_3	4×10^{-3} 8×10^{-5}	2×10^{-3} 8×10^{-5}
Detected fluo helicity ξ_f	67.9 Hz modulation	spurious modulation in unpol. fluo. signal	8×10^{-4}	
Electric field **E**	random reversal every 20 s	change in modulus in direction	$\lesssim 10^{-4}$ $\lesssim 3 \times 10^{-4}$	$\lesssim 5 \times 10^{-5}$

In order to avoid such quasi-coincidences a careful analysis of the modulation spectrum must be performed prior to choosing values for the rotation frequencies. Subsequent stabilization of these frequencies is necessary. A quasi-coincidence affecting *only one* parity channel increases the noise in this channel. This is detected by testing the *equality of the noises* in the two channels. A quasi-coincidence affecting *both channels* nearly equally is detected by testing the *correlation* between the two channels. These two tests are incorporated in the real time data processing (part III).

iv) Narrow isolated peaks (typically 2 per min, typical duration : detector's $RC \simeq 10^{-3}$ s), high above the normal noise level. They originate mainly in cosmic muons, against which the lead shielding is helpless.

2.9.3 *Practical realization.* — Prior to lock-in detection of the small modulations of § 2.9.2 ii) the detector's output signal is cleared of the large modulations and of the muons peaks, so as to avoid saturation in the lock-in amplifiers. The large modulations of § 2.9.2 i), as well as the largest stray modulation (at frequency $2\,\omega_f$; amplitude 3×10^{-2}) are rejected by notch amplifiers. The muon peaks are rejected by a specially designed active filter working as follows. After rejection of the large modulations, the modulus of the remaining signal (nearly mere noise) is compared to a threshold value equal to three times the rms value of the signal for the past second. If the signal modulus exceeds the threshold, a multiplexer is switched so that the signal is replaced by the threshold value (with appropriate sign) until the true signal falls back below the threshold. The threshold value is elaborated from the *processed* signal, which is thus « truncated at $\pm$ 3 rms deviations in a self-consistent way ». In this procedure, the far wings of a pure Gaussian noise distribution (without muon peaks) are truncated. This artificial noise reduction (1.5 %) has been corrected for in the final results.

Reference waveforms for lock-in detection at various frequency combinations are prepared by combining the three basic reference waveforms output by the rotors (§ 2.2.3). Only two waveforms are mixed at a time, using an analog multiplier. Among the two resulting frequencies, the undesired one is rejected by a notch amplifier. (In case of drift detuning, this method introduces no phase shift on the desired frequency, in contrast with selecting it with a selective amplifier). Possible detuning is checked from time to time but is rarely appreciable. Detuning of the parity channels would anyway be both detected and eliminated in the periodic calibration sequences.

Proper initial phase setting of the lock-in amplifiers is achieved using large, well understood atomic signals which appear, in modified experimental configurations, at the same frequencies as the signals of interest and with the same phases (or $\pi/2$ out-of-phase). Subsequent phase drifts are detected in real time in auxiliary measurements. Corrections are few and small ($< 5°$).

2.10 DIGITAL INTEGRATION. — The outputs of the lock-in amplifiers are fed into a home-made 32-channel digital integrator, where they are sampled (every 32 ms), digitized and accumulated. After 16 s (« live time »), integration stops for 4 s (« dead time ») to allow parameter reversal(s) and subsequent restabilization. Meanwhile the program reads the integrator. During the PV measurements two signs η (electric field) and η' (Pockels voltage) are reversed in $2^2 = 4$ successive live times. The program computes the PV asymmetry defined as :

$$\mathcal{A}^{pv} = \sum_{\eta\eta'} \eta\eta'(\mathcal{F}_{e+f} + \mathcal{F}_{e-f})/4 \,|\, \mathcal{F}_{e+b} \,| \qquad (2.9)$$

where $\mathcal{F}_{i\pm j}$ denotes the amplitude detected at frequency $\omega_i \pm \omega_j$ with the proper phase. $\mathcal{A}^{pv}$ is twice the η-odd, η'-odd polarization ratio of the fluorescence light. It is in principle equal to the PV atomic polarization, proportional to Im $E_1^{pv}/\alpha E$ or Im $E_1^{pv}/\beta E$ in the $\Delta F = 0$ or 1 hfs component respectively. As explained in § 1.3.2, the PV asymmetry is calibrated by reference to the polarization $P^{(2)}$ measured at the peak of the $4 \to 4$ component in a magnetic field $\mathbf{H}_0 /\!/ \mathbf{E}$. The corresponding fluorescence signal $\mathcal{F}^{(2)}$, proportional to $\xi\xi_f$ like $\mathcal{F}^{pv}$, gives rise to modulations at the same frequencies and phases. Their large amplitudes are detected with the same electronics, except an accurately calibrated divider ($\div$ 100), inserted before the lock-in amplifiers to avoid changing their sensitivities (and calibrations). Signal $\mathcal{F}^{(2)}$ also allows easy phase adjustment in order to detect $\xi\xi_f$. During calibration measurements, three signs (η, η', η'' sign of $\mathbf{H}_0$) are reversed in $2^3 = 8$ successive live times. The program computes the quantity :

$$C = \sum_{\eta\eta'\eta''} \eta'\,\eta''(\mathcal{F}_{e+f} + \mathcal{F}_{e-f})/4 \,|\, \mathcal{F}_{e+b} \,|\,. \qquad (2.10)$$

But for the replacement of η by η'', (2.9) and (2.10) are identical. This is why the calibration standard C is measured in exactly the same way as the quantity of interest $\mathcal{A}^{pv}$, except that $\mathbf{H}_0$ instead of $\mathbf{E}$ is reversed.

Calibration of $\mathcal{A}^{pv}$ by C finally leads to the quantity

$$\mathcal{A}^{pv}/C = P^{pv}_{FF'}/P^{(2)}_{44} \propto \begin{cases} \text{Im } E_1^{pv}/\beta E & \text{in Exp. 1 } (4 \to 4) \\ (\text{Im } E_1^{pv}/\beta E).(\alpha/\beta) & \text{in Exp. 2 } (3 \to 4) \end{cases}. \qquad (2.11)$$

It turns out that the omitted leading factors in (2.11) are of same sign (App. C, Eqs. (C.7)). Consequently, since α/β is observed to be negative [28, 45], $\mathcal{A}^{pv}/C$ is of opposite sign in Exp. 1 and Exp. 2.

Let us note that the interpretation of the measured ratio $\mathcal{A}^{pv}/C$ in terms of the PV parameter Im E_1^{pv}/β is quite direct. In particular the absolute sign determination requires only the knowledge of the relative orientation of $\mathbf{E}$ and $\mathbf{H}_0$ (in a given state of the relays that reverse η and η'').

A complete description of the data acquisition sequences, including real time control of systematic effects, is the object of § 4 (part III).

2.11 CHOICE OF OPERATING CONDITIONS FOR OPTIMUM SIGNAL/NOISE RATIO. — An important step has been to reach conditions where the dominant noise is the photon noise of the atomic fluorescence. The crucial parameter is the electric field magnitude. Below some value E_{min} the signal-independent noise is dominant. This noise contains several contributions :

— photon noise of the thermal IR radiation of the oven ;

— photon noise of the non-resonant fluorescence induced by Cs-Cs collisions ;

— intrinsic noise of the detector.

Once $|E| > E_{min}$ the photon noise ($\propto E$) of the Stark-induced fluorescence ($\propto E^2$) dominates. The S/N ratio ($\propto$ (Im $E_1^{pv}.E)/E$) is then independent of E. Further increase of $|E|$ would needlessly reduce the PV asymmetry ($\propto$ Im E_1^{pv}/E) and favour electric discharges, prone to appear in view of the helium atmosphere and of the intense laser irradiation. Successive improvements (in noise reduction : oven design, filter, detector ; or in statistics increase : laser intensity, multipass efficiency, detector size) resulted in successive reductions of E_{min}. Increase of the caesium pressure is in practice limited to 50-100 mtorr ($T \simeq 200$ °C) by depolarization in Cs-Cs collisions, by increase of oven radiation and of collision-induced fluorescence ($\propto P_{Cs}^2$), and by Cs vapour density instabilities.

Typical operating conditions in both Exp. 1 and Exp. 2 are shown in table VII. In both cases the dominant noise was the photon noise of the resonant fluorescence. The reason for the higher Stark field for Exp. 2 is that E_{min} is one order of magnitude higher, simply because the $\Delta F = 1$ component is a factor $(\alpha/\beta)^2 \approx 100$ smaller. The higher field required lower caesium and helium pressures to exclude any risk of discharge.

To maintain optimum S/N ratio throughout data acquisition, careful setting and manual readjustments of the laser beam intensity and direction, of the multipass and of the Cs vapour pressure were performed (during interruptions). The criterion was the instantaneous estimation of the noise, continuously

Table VII. — *Typical experimental parameters.*

	Exp. 1	Exp. 2
Laser power at laser output (mW)	500	
at cell entrance (mW)	200	250
or photon flux (ph/s)	6×10^{17}	7.5×10^{17}
Modulation frequencies (Hz) characteristic		
of the incident polarization :	$\omega_e/2\pi = 460.8$	$\omega_b/2\pi = 342.6$
of the detected polarization :	$\omega_f/2\pi = 67.9$	
Multipass : number of passes 2 N	~ 120 to 140	
size of ellipse axes : $/\!/\mathbf{E}$ (mm)	2	1-1.5
$\perp \mathbf{E}$	24	22
Mirror parameters : losses	1×10^{-3}	
birefringence : return mirror	3×10^{-6}	1×10^{-5} (rotated)
(rad) input mirror	6×10^{-6}	1×10^{-5}
off-normal incidence	1.3×10^{-5}	
Global birefringence (rad)	$\lesssim 4 \times 10^{-3}$	$\lesssim 2 \times 10^{-3}$
Cell voltage (V/cm)	100 to 140	600 to 700
Cs number density (10^{15} at/cm^3)	1.6 (200 °C)	0.8 (185 °C)
He pressure (torr)	0.35	0.15
Length of the sensitive area (mm)	9	25
Photon collection efficiency	10^{-3}	
Detected fluorescence flux (ph/s)	1.2×10^9	4×10^8
Unmodulated flux :		
— from Cs-Cs collisions	1.2×10^8	6×10^7
— from oven thermal radiation	1.5×10^8	

displayed by the « noisemeter » (described in the next paragraph) and compared to the optimum level expected from the signal magnitude. However, the average noise level quoted with the results is estimated from the dispersion of the data themselves, not from the noisemeter.

Finally, the typical integration time for unit S/N ratio was in both measurements $\simeq$ 6 h, corresponding to a real operating time of $\simeq$ 9 h once dead times and controls are included.

2.12 THE « NOISEMETER ». — We have imagined a « noisemeter » (for its rôle see end of § 2.11). This is a device that displays a nearly instantaneous measurement of the noise superimposed with a signal. A prerequisite is that around some frequency ν the signal power is negligible with respect to the noise power.

The first stage is a primitive lock-in amplifier, whose reference is an internal oscillator at frequency ν. This stage transfers the noise of the frequency band $[\nu - \Delta\nu, \nu + \Delta\nu]$ (assumed to contain no signal) to the band $[-\Delta\nu, +\Delta\nu]$. $\Delta\nu$ is chosen through proper setting of the output filter time constant. A second stage digitizes N samples X_i of the output of the first one, and computes the quantity $\{[\sum X_i^2 - (\sum X_i)^2/N]/(N-1)\}^{1/2}$. Provided the N samples are distributed over a period of time large as compared to $1/\Delta\nu$, this quantity is the rms value of X for the considered period, i.e. the noise voltage in the band $[\nu - \Delta\nu, \nu + \Delta\nu]$ for this period.

In our real case, since signals and stray modulations all appear at definite frequencies, a frequency ν with mere noise is easily found. In practice $\nu = 1$ kHz; sampling occurs every 2.5 ms; $\Delta\nu$ (with 12 dB/OC filtering) can be selected from 8 to 250 Hz; N can be selected from 2^0 to 2^{12}.

3. Conclusion.

As seen in Section 1 the fluorescence signal contains numerous contributions of different specific signature. The description of the apparatus (Sect. 2) has reflected our concern in ensuring the quality of the geometry and of the reversals. This is crucial to extract each signal unambiguously. We insisted on the fact that in the ideal configuration a single defect is not sufficient to simulate P^{pv}. The next crucial step will be to discuss how conspiration between two (or more) imperfections can generate a false parity signal. Simultaneously we will analyse how one can assess the magnitude of each expected systematic effect by combining different data available in the atomic signal. This will be the subject of the second part of our paper.

Acknowledgments.

We are very grateful to Claude Bouchiat for constant interest and for numerous stimulating discussions concerning the theoretical interpretation of all this work. It is a pleasure to thank Larry Hunter for his enthusiastic participation during the final stage of this experiment. His contribution in putting into shape various experimental procedures described in this paper, is gratefully acknowledged. We are grateful to André Clouqueur for the design of numerous electronics and to Gérard Trénec for the design of various mechanics. We thank glassblower Georges Tota of SVT ([7]) and the craftsmen of the ENS workshop for delicate or even acrobatic realizations.

Appendix A

In this appendix we give a derivation of : (i) the population and electronic spin polarization of the excited state; (ii) the fluorescence signals emitted in the 7S - $6P_{1/2}$ decay. We consider the most general configuration. The 6S, $F \to 7S$, F' hfs component is excited in an electric field $\mathbf{E}$ of arbitrary direction, by a resonant laser beam of arbitrary complex polarization vector $\boldsymbol{\varepsilon}$ propagating along the unit vector $\hat{\mathbf{k}}$. The 6S, $F \to 7S$, F' transition amplitudes can be obtained from the effective transition matrix T acting on the electronic spin states, already defined in Section 1 (Eq. (1.10)) :

$$T = a\,\mathbb{1} + \mathbf{b}\cdot\boldsymbol{\sigma}\,. \tag{A.1}$$

$\mathbb{1}$ is the unit two-by-two matrix and the component of $\boldsymbol{\sigma}$ are the three Pauli matrices;

$$a = \alpha\mathbf{E}\cdot\boldsymbol{\varepsilon}\,, \tag{A.2}$$

$$\mathbf{b} = i\beta\mathbf{E}\times\boldsymbol{\varepsilon} - M_1'\,\hat{\mathbf{k}}\times\boldsymbol{\varepsilon} + i\,\mathrm{Im}\,E_1^{pv}\,\boldsymbol{\varepsilon}\,. \tag{A.3}$$

Since the transition is so highly forbidden, the initially unpolarized ground state remains practically unpolarized. Stimulated emission is totally negligible with respect to spontaneous emission, and optical coherences between the 6S and 7S states can be ignored. The restriction ρ of the density operator to the 7S state is written, up to a normalization factor :

$$\rho = P_{7S}\,T\rho_g\,T^+\,P_{7S}\,,$$

where ρ_g is the restriction of the density operator to the 6S (ground) state assumed at thermal equilibrium, and P_{7S} is the projector on the 7S state. We assume that the (single-mode, cw) laser selects one hfs component 6S, $F \to 7$ S, F'. We also assume that no magnetic field is applied, so the F and F' sublevels remain degenerate. The density matrix is thus given by :

$$\rho = P_{F'}\,TP_F\,T^+\,P_{F'}\,, \tag{A.4}$$

where P_F is the projector on the F sublevel. In order to compute the 7S population and its electronic

([7]) Société de Verrerie et de Thermométrie, 135, rue du Théâtre, 75015 Paris, France.

spin polarization proportional to Tr ρ and Tr $\rho\boldsymbol{\sigma}$ respectively, we apply the Wigner-Eckart theorem to the spin operator $\boldsymbol{\sigma}$ acting in the hyperfine subspace F :

$$P_F\,\boldsymbol{\sigma} P_F = 2\,g_F\,P_F\,\mathbf{F}\,, \quad \text{where} \quad g_F = 2(F - I)/(2\,I + 1)\,. \tag{A.5}$$

After some elementary algebra, using equations (A.1)-(A.5) we obtain for the $\Delta F = F' - F$ transition :

$$\text{Tr}\,\rho = n_{F'}(\delta_{FF'}\,aa^* + h_{FF'}\,\mathbf{b}\cdot\mathbf{b}^*)\,, \tag{A.6}$$

$$\text{Tr}\,\rho\boldsymbol{\sigma} = n_{F'}\,p_{F'}[\delta_{FF'}\,(a\,\mathbf{b}^* + a^*\,\mathbf{b}) + ig_{FF'}\,\mathbf{b}\times\mathbf{b}^*]\,, \tag{A.7}$$

where

$$\left.\begin{aligned} n_{F'} &= 2\,F' + 1 \quad \text{(multiplicity of the } F' \text{ level)}\,; \\ p_{F'} &= (1 + 2\,g_{F'})/3 = (4\,F' - 2\,I + 1)/3(2\,I + 1)\,; \\ \delta_{FF'} &= 1\,, \quad \text{if} \quad \Delta F = 0 \\ &= 0\,, \quad \text{if} \quad \Delta F = \pm 1\,; \\ h_{FF'} &= (1 + 2\,g_{F'})/3 \quad \text{and} \quad g_{FF'} = g_{F'}\,, \qquad \text{if} \quad \Delta F = 0\,; \\ &= 2(1 - g_{F'})/3 \qquad\qquad = 1 - g_{F'}\,, \quad \text{if} \quad \Delta F = \pm 1\,. \end{aligned}\right\} \tag{A.8}$$

We now insert equations (A.2) and (A.3) in (A.6) and (A.7). We thus obtain :

$$\text{Tr}\,\rho = n_{F'}\,\{\,\delta_{FF'}\,\alpha^2\,|\,\mathbf{E}\cdot\hat{\boldsymbol{\varepsilon}}\,|^2 + h_{FF'}[\beta^2\,|\,\mathbf{E}\times\hat{\boldsymbol{\varepsilon}}\,|^2 + (M_1' + \xi\,\text{Im}\,E_1^{\text{pv}})^2]\,\}\,|\,\boldsymbol{\varepsilon}\,|^2 \tag{A.9}$$

$$\begin{aligned}\text{Tr}\,\rho\boldsymbol{\sigma} = n_{F'}\,p_{F'}\,\{\,&\text{Im}\,E_1^{\text{pv}}(\delta_{FF'}\,\alpha + g_{FF'}\,\beta)\,(\mathbf{E}\times\xi\hat{\mathbf{k}}) - [\delta_{FF'}\,\alpha\beta E^2\,\xi\hat{\mathbf{k}} - (\delta_{FF'}\,\alpha + g_{FF'}\,\beta)\,(\mathbf{E}\cdot\xi\hat{\mathbf{k}})\,\beta\mathbf{E}] + \\ &+ M_1'\,2\,\text{Re}\,[\delta_{FF'}\,\alpha(\hat{\boldsymbol{\varepsilon}}\cdot\mathbf{E})\,(\hat{\boldsymbol{\varepsilon}}^*\times\hat{\mathbf{k}}) + g_{FF'}\,\beta(\hat{\mathbf{k}}\times\hat{\boldsymbol{\varepsilon}}\cdot\mathbf{E})\,\hat{\boldsymbol{\varepsilon}}^*] + g_{FF'}(M_1' + \xi\,\text{Im}\,E_1^{\text{pv}})^2\,\xi\hat{\mathbf{k}}\,\}\,|\,\boldsymbol{\varepsilon}\,|^2\end{aligned} \tag{A.10}$$

where $\hat{\boldsymbol{\varepsilon}} = \boldsymbol{\varepsilon}/|\,\boldsymbol{\varepsilon}\,|$ and ξ represents the helicity of the beam, defined in equation (1.11). Introducing the electronic polarization $\mathbf{P} = \text{Tr}\,\rho\boldsymbol{\sigma}/\text{Tr}\,\rho$, we rewrite (A.10) in the form :

$$\mathbf{P} = \mathbf{P}^{\text{pv}} + \mathbf{P}^{(2)} + \mathbf{P}^{(1)} + \mathbf{P}^{(0)}\,. \tag{A.11}$$

The four contributions thus defined correspond to the four successive terms in (A.10). Each of them originates in interference between a different pair of terms in (A.2) and (A.3).

We now turn to the fluorescence signals associated with the spontaneous decay on the $7S_{1/2}$ - $6P_{1/2}$ line. The fluorescence light transmitted by an analyser selecting the polarization $\boldsymbol{\varepsilon}_f$ is :

$$\mathcal{F} \propto \text{Tr}\,\{\,P_{6P_{1/2}}\,\mathbf{d}\cdot\boldsymbol{\varepsilon}_f^*\,\rho\mathbf{d}\cdot\boldsymbol{\varepsilon}_f\,\}\,,$$

where $P_{6P_{1/2}}$ is the projector on the final state. Applying the Wigner-Eckart theorem to the matrix elements of $\mathbf{d}$ between two $j = 1/2$ states, we obtain, up to a constant :

$$\mathcal{F} \propto \text{Tr}\,\{\,\boldsymbol{\sigma}\cdot\boldsymbol{\varepsilon}_f^*\,\rho\boldsymbol{\sigma}\cdot\boldsymbol{\varepsilon}_f\,\} = (\boldsymbol{\varepsilon}_f\cdot\boldsymbol{\varepsilon}_f^*)\,\text{Tr}\,\rho + i(\boldsymbol{\varepsilon}_f\times\boldsymbol{\varepsilon}_f^*)\cdot\text{Tr}\,\rho\boldsymbol{\sigma}\,.$$

As expected since the hfs of the 7S - $6P_{1/2}$ line is not resolved, the fluorescence light involves only the population and electronic spin polarization of the excited state. Observation takes place along the direction $\hat{\mathbf{k}}_f$ through an analyser transmitting the polarization $\boldsymbol{\varepsilon}_f$ of helicity $\xi_f = \text{Im}\,(\boldsymbol{\varepsilon}_f^*\times\boldsymbol{\varepsilon}_f\cdot\hat{\mathbf{k}}_f)/\boldsymbol{\varepsilon}_f\cdot\boldsymbol{\varepsilon}_f^*$. Therefore :

$$\mathcal{F} \propto \text{Tr}\,\rho + \xi_f\,\text{Tr}\,\rho\boldsymbol{\sigma}\cdot\hat{\mathbf{k}}_f\,.$$

The circular polarization ratio p_c of the fluorescence light emitted along $\hat{\mathbf{k}}_f$ is thus :

$$p_c = \text{Tr}\,\rho\boldsymbol{\sigma}\cdot\hat{\mathbf{k}}_f/\text{Tr}\,\rho = \mathbf{P}\cdot\hat{\mathbf{k}}_f \tag{A.12}$$

which is simply the electronic polarization ratio along direction $\hat{\mathbf{k}}_f$. Let us denote $\mathcal{F}_u$ and $\mathcal{F}_p$ the signals respectively associated with the unpolarized and polarized components of the fluorescence light; then

$$\mathcal{F} = \mathcal{F}_u + \mathcal{F}_p \quad \text{with} \quad \mathcal{F}_u \propto \text{Tr}\,\rho \tag{A.13}$$

$$\text{and} \quad \mathcal{F}_p \propto \xi_f\,\text{Tr}\,\rho\boldsymbol{\sigma}.\mathbf{k}_f = \xi_f\,\mathbf{P}.\hat{\mathbf{k}}_f\,\mathcal{F}_u\,. \tag{A.14}$$

Inserting (A.11) in (A.14), we distinguish in the polarized fluorescence signal $\mathcal{F}_p$ four contributions $\mathcal{F}^{\text{pv}}$, $\mathcal{F}^{(2)}$,

$\mathcal{F}^{(1)}$, $\mathcal{F}^{(0)}$, respectively associated with the four successive terms of (A.10). We obtain :

$$\mathcal{F}_p = \mathcal{F}^{pv} + \mathcal{F}^{(2)} + \mathcal{F}^{(1)} + \mathcal{F}^{(0)} \tag{A.15}$$

with :

$$\mathcal{F}^{pv} = \mathcal{F}_u \mathbf{P}^{pv} \cdot \xi_f \hat{\mathbf{k}}_f = n_{F'} p_{F'} \operatorname{Im} E_1^{pv} (\delta_{FF'} \alpha + g_{FF'} \beta) \mathbf{E} \times \xi\hat{\mathbf{k}} \cdot | \varepsilon |^2 \cdot \xi_f \hat{\mathbf{k}}_f \tag{A.16}$$

$$\mathcal{F}^{(2)} = \mathcal{F}_u \mathbf{P}^{(2)} \cdot \xi_f \hat{\mathbf{k}}_f = n_{F'} p_{F'} [- \delta_{FF'} \alpha\beta E^2 \xi\hat{\mathbf{k}} + (\delta_{FF'} \alpha + g_{FF'} \beta) (\mathbf{E} \cdot \xi\hat{\mathbf{k}}) \beta\mathbf{E}] | \varepsilon |^2 \cdot \xi_f \hat{\mathbf{k}}_f \tag{A.17}$$

$$\mathcal{F}^{(1)} = \mathcal{F}_u \mathbf{P}^{(1)} \cdot \xi_f \hat{\mathbf{k}}_f = n_{F'} p_{F'} M_1' \, 2 \operatorname{Re} [\delta_{FF'} \alpha(\varepsilon \cdot \mathbf{E}) (\varepsilon^* \times \hat{\mathbf{k}}) + g_{FF'} \beta(\hat{\mathbf{k}} \times \varepsilon \cdot \mathbf{E}) \varepsilon^*] \cdot \xi_f \hat{\mathbf{k}}_f \tag{A.18}$$

$$\mathcal{F}^{(0)} = \mathcal{F}_u \mathbf{P}^{(0)} \cdot \xi_f \hat{\mathbf{k}}_f = n_{F'} p_{F'} g_{FF'} (M_1' + \xi \operatorname{Im} E_1^{pv})^2 \xi\hat{\mathbf{k}} | \varepsilon |^2 \cdot \xi_f \hat{\mathbf{k}}_f \tag{A.19}$$

Equations (A.13) and (A.9) lead to :

$$\mathcal{F}_u = n_{F'} \{ \delta_{FF'} \alpha^2 | \mathbf{E} \cdot \hat{\varepsilon} |^2 + h_{FF'} [\beta^2 | \mathbf{E} \times \hat{\varepsilon} |^2 + (M_1' + \xi \operatorname{Im} E_1^{pv})^2] \} | \varepsilon |^2 . \tag{A.20}$$

In the limit case $E = 0$, (A.16)-(A.18) show that $\mathcal{F}^{pv}$, $\mathcal{F}^{(2)}$ and $\mathcal{F}^{(1)}$ vanish. From (A.12) the circular polarization ratio of the fluorescence light then reduces to :

$$p_c(E = 0) = \mathbf{P}^{(0)}(E = 0) \cdot \hat{\mathbf{k}}_f$$

with, from (A.19)-(A.20) and definitions (A.8)

$$\mathbf{P}^{(0)}(E = 0) = p_{F'} (g_{FF'}/h_{FF'}) \cdot \xi\hat{\mathbf{k}} \begin{cases} = g_{F'} \xi\hat{\mathbf{k}}, & \text{if } \Delta F = 0, \\ = \frac{1}{2}(1 + 2 g_{F'}) \cdot \xi\hat{\mathbf{k}}, & \text{if } \Delta F = \pm 1. \end{cases}$$

$\mathbf{P}^{(0)}(E = 0)$ is the electronic polarization in zero electric field.

Since $| E_1^{pv}/M_1' | \sim 10^{-4} \ll 1$, and since in addition in the conditions of the PV measurements the $\xi M_1' \operatorname{Im} E_1^{pv}$ interference terms cancel out (by use of a beam multipass), the approximation $(M_1' + \xi \operatorname{Im} E_1^{pv})^2 \simeq M_1'^2$ is fully justified in the present context in both (A.19) and (A.20).

Remark : *Collision-induced absorption.* — Instead of being polarized by an external electric field, the Cs atom can be polarized by interaction with another atom during a collision. This process is represented in the transition matrix by a new contribution :

$$T_b = A\hat{\mathbf{n}} \cdot \varepsilon + iB\sigma \times \hat{\mathbf{n}} \cdot \varepsilon ,$$

analogous to the Stark-induced contribution $\alpha\mathbf{E} \cdot \varepsilon + i\beta\sigma \times \mathbf{E} \cdot \varepsilon$. We expect B/A to be comparable with $\beta/\alpha \simeq 1/10$. The main difference with the Stark-induced terms is that symmetry commands the unit vector $\hat{\mathbf{n}}$ to lie along the internuclear axis, whose random direction is distributed isotropically. As a result of the short interaction duration, this process is characterized by a spectral width much larger than the hfs splittings. The first term in T_b contributes to the unpolarized background observed in $\mathcal{F}_u$ and discussed in § 1.2.1. Interference between the A and B terms leads to a spin polarization along $\hat{\mathbf{k}}$, yielding a non-resonant, E-independent polarized fluorescence signal :

$$\mathcal{F}_b = \sum_{F'} n_{F'} p_{F'} B_p^2 | \varepsilon |^2 \xi\hat{\mathbf{k}} \cdot \xi_f \hat{\mathbf{k}}_f \tag{A.21}$$

where $B_p^2 = \langle - AB \rangle$. The sum runs over the 2 hf levels of the excited state. These are assumed to be populated with the statistical weights $n_{F'} = 2F' + 1$ whatever the laser detuning within the hfs profile. We have experimental evidence that Cs-He collisions contribute to a weak signal of this kind [21]. On the contrary no contribution from Cs-Cs collisions could be evidenced. $\mathcal{F}_b/\mathcal{F}_u$ is linear in the He pressure for $P_{He} < 0.5$ torr and independent of the Cs pressure. In the conditions of the PV measurements, its observed size corresponds to $| B_p/\alpha | \simeq 5$ V/cm at $P_{He} \simeq 0.35$ torr.

A discussion of the physical significance of the results obtained in this appendix is given in the text (Sect. 1.2).

Appendix B.

In this appendix, we study new terms which appear in the expression of the fluorescence signal when a magnetic field $\mathbf{H}$ is present in addition to the Stark field $\mathbf{E}$. The details of the calculation can be found in references [37, 38]. Here we only outline the assumptions and the results *relevant to our* PV *experiments.* In these experiments, only weak magnetic fields ($H \leqslant 10$ G) are involved, so that the Zeeman splitting

$$\mu_B H/h(I + 1/2) = 0.375 \times H \text{ (in Gauss)} \quad \text{(MHz)} \tag{B.1}$$

is at most of the order of the natural linewidth ($1/2\pi\tau_{7S} \simeq 3$ MHz).

According to a rigorous analysis, the magnetic field acts in two ways which can be thought of as two successive steps in time :

(i) the magnetic field gives rise to new terms in the population and spin polarization of the upper state;

(ii) through Hanle effect, the magnetic field then affects the direction and size of the stationary spin polarization deduced from all (new or old) source terms.

To create new terms, the magnetic field acts through two mechanisms : it perturbs either the eigenstates (hyperfine mixing), or the eigenenergies (lifting of level degeneracy). Since the Zeeman splitting (B.1) remains small compared to the hfs splittings of the 6S and 7S states

$$\omega_6/2\pi = 9\,193 \text{ MHz} \quad \text{and} \quad \omega_7/2\pi = 2\,184 \text{ MHz}, \tag{B.2}$$

and to the Doppler width ($\sim$ 750 MHz), a first-order perturbative treatment is justified. To this extent, the two mechanisms simply add and can be treated separately. They are expected to give rise to qualitatively identical effects : these correspond in both cases to the new invariant physical quantities which can be constructed when a magnetic field is added to the preexistent configuration. Besides, the effect of eigenenergy perturbation vanishes identically when the laser frequency is tuned to the centre of a hfs line, which is in principle the case in our PV experiments. Consequently, we expect the lifting of level degeneracy to lead at most to corrections to the hyperfine mixing effects.

In the evolution of the spin polarization in the $7S_{1/2}$, F' hyperfine sublevel, the effect of the nuclear spin is simply described through the g-factor $2\,g_F$ (Eq. (A.5)), yielding a Hanle width :

$$\Delta H = \hbar/(2 \mid g_{F'}\,\mu_B \mid \tau_{7S}) \sim 10 \text{ Gauss}. \tag{B.3}$$

In this respect, hf mixing can be shown to contribute only to corrections of second order in $\mu_B H/\hbar\omega_{6,7}$, which remain $\leqslant 10^{-4}$ at the field magnitudes involved in practice.

Hereafter no assumption is made concerning the direction of the Stark field **E** (except special mention).

B.1 HYPERFINE MIXING (AND DEGENERACY LIFT) EFFECTS. — We deal separately with the new ξ-independent and ξ-dependent effects.

a) *ξ-independent effects.* — Two new components $\mathbf{P}_{hf}$ and $\mathbf{P}^x_{hf}$ are created in the 7S spin polarization, along **H** and normal to **H** respectively. In view of their symmetry (see below), they are not potential sources of systematics in the PV measurement, but prove useful for calibration purposes. Therefore, we explicit the results only for the configuration of practical interest, i.e. $\mathbf{H} \perp \hat{\mathbf{k}}$. (In a field **H** of arbitrary direction, the effects are similar, only their size is changed.) Besides, we consider here only the contributions odd under reversal of **H**, since they provide the best experimental characterization together with complete information. With the same normalization as in appendice A, the H-odd contributions in the polarized fluorescence signal, detected along $\hat{\mathbf{k}}_f$, are found to be :

$$\mathcal{F}_{hf} = \mathcal{F}_u\,\xi_f\,\mathbf{P}_{hf}\cdot\hat{\mathbf{k}}_f = n_{F'}\,j_{F'}\left[\delta_{FF'}\,\alpha^2 \mid \mathbf{E}\cdot\boldsymbol{\varepsilon} \mid^2 + \left(j'_{FF'} + j''_{FF'}\,\frac{\delta\omega.\omega_7}{\Omega_D^2}\right)\beta^2 \mid \mathbf{E}\times\boldsymbol{\varepsilon} \mid^2\right]\cdot\left|\frac{\mu_B H}{\hbar\omega_7}\right|\hat{\mathbf{H}}.\xi_f\,\hat{\mathbf{k}}_f \tag{B.4}$$

$$\mathcal{F}^x_{hf} = \mathcal{F}_u\,\xi_f\,\mathbf{P}^x_{hf}\cdot\hat{\mathbf{k}}_f = n_{F'}\,k_{FF'}\left[\left(\frac{1}{\omega_7}-\frac{1}{\omega_6}\right) + \delta_{FF'}\cdot\frac{2\,g_{F'}}{1-g_{F'}}\cdot\frac{\delta\omega}{\Omega_D^2}\right]\times$$
$$\times\left|\frac{\mu_B H}{\hbar}\right|\cdot\left[1+\left(\frac{H}{\Delta H}\right)^2\right]^{-1}\cdot\alpha\beta\,\mathrm{Re}\left[(\mathbf{E}\cdot\boldsymbol{\varepsilon})\,(\mathbf{E}\times\boldsymbol{\varepsilon}^*)\right]\times\hat{\mathbf{H}}.\xi_f\,\hat{\mathbf{k}}_f, \tag{B.5}$$

with

$$\left.\begin{aligned} j_{F'} &= \tfrac{4}{3}(1-g_{F'})\,\mathrm{sgn}\,g_{F'}\,; \\ k_{FF'} &= \tfrac{2}{3}(1+2\,g_{F'})\,(1-g_{F''})\,\mathrm{sgn}\,g_F = 2\,p_{F'}(1-g_{F'})\,\mathrm{sgn}\,g_F\,; \end{aligned}\right\} \tag{B.6}$$

$$\text{if } \Delta F = 0, \qquad \left.\begin{aligned} j'_{FF'} &= \frac{1}{10}(1+2\,g_{F'})\left[(3+4\,g_F) - (1+8\,g_{F'})\frac{\omega_7}{\omega_6}\right]; \\ j''_{FF'} &= -\frac{1+2\,g_{F'}}{1-g_{F'}}\cdot g_{F'}^2\,; \end{aligned}\right\} \tag{B.7a}$$

$$\text{if } \Delta F = \pm 1, \qquad \left.\begin{aligned} j'_{FF'} &= \frac{1}{10}\left[(1-2\,g_{F'})(7+4\,g_{F'}) + (1+2\,g_{F'})(1+8\,g_{F'})\frac{\omega_7}{\omega_6}\right]; \\ j''_{FF'} &= \frac{1}{5}(4-3\,g_{F'})(1+2\,g_{F'})\,. \end{aligned}\right\} \tag{B.7b}$$

In these expressions, $\delta\omega = \omega_L - \omega_{6F,7F'}$ is the laser detuning from the centre of the 6S, $F \to 7S$, F' hfs line; $\Omega_D = \omega_L(2\,kT/M_{Cs}\,c^2)^{1/2}$ corresponds to a FWHM Doppler width $2(\mathrm{Log}\,2)^{1/2}\,\Omega_D/2\pi \approx 750$ MHz. In equation (B.5), the factor $[1+(H/\Delta H)^2]^{-1}$ originates in Hanle effect which affects only $\mathbf{P}^x_{hf}$ created transverse

to **H**. Both signals are quadratic in **E** and involve definite components of the *linear* polarization of the laser beam. In the particular case $\mathbf{E} \perp \hat{\mathbf{k}}$, $\mathcal{F}_{hf}$ depends on that component whose axes are $/\!/\mathbf{E}$ and $\perp \mathbf{E}$; $\mathcal{F}^{x}_{hf}$ depends on that one whose axes lie at $\pm$ 45° from **E**, and originates in a spin polarization initially created along $\hat{\mathbf{k}} \times \hat{\mathbf{H}}$. Note that the effect of laser detuning is very small in $\mathcal{F}_{hf}$ when $F = F'$ (in so far as $j''_{FF}(\omega_7\ \delta\omega/\Omega_D^2)\ \beta^2/\alpha^2 \sim 2 \times 10^{-6}\ \delta\omega/2\pi$ (MHz)) and is totally absent in $\mathcal{F}^{x}_{hf}$ when $F \neq F'$. In (B.4) and (B.5), M'^2_1 terms are omitted since their contribution is negligible ($\leqslant 10^{-3}$) at the Stark field used in practice.

b) *ξ-dependent effects.* — Such effects appear both in the 7S population (through $\alpha\beta$ interference) and in the spin-polarization (through $\alpha M'_1$ and $\beta M'_1$ interferences), when the magnetic field has a non-zero component along the beam. The corresponding new term in the unpolarized fluorescence signal of the 6S, $F \to 7S$, F' component is written :

$$\mathcal{F}_{u,hf} = -\frac{2}{3} n_{F'}(1 - g_{F'}) \cdot \left|\frac{\mu_B H}{\hbar}\right| \cdot \left(\frac{\operatorname{sgn} g_F}{\omega_6} + \frac{\operatorname{sgn} g_{F'}}{\omega_7}\right) \alpha\beta E^2 (\hat{\mathbf{H}} \cdot \xi\hat{\mathbf{k}}) \mid \varepsilon \mid^2 . \tag{B.8}$$

(No contribution arises from the lifting of level degeneracy [38]).

In a magnetic field **H** small as compared with the Hanle width (e.g. in a stray field), the new term in the polarized fluorescence signal is :

$$\mathcal{F}^{(1)}_{hf}(H \ll \Delta H) = \mathcal{F}_u\, \mathbf{P}^{(1)}_{hf} \cdot \xi_f\, \hat{\mathbf{k}}_f = -\, n_{F'}\, p_{F'}(\operatorname{sgn} g_F) \left|\frac{\mu_B H}{\hbar \omega^*_{hf}}\right| (\hat{\mathbf{H}} \cdot \hat{\mathbf{k}})\, M'_1\, \alpha \mathbf{E} \times \xi\hat{\mathbf{k}} \cdot \xi_f\, \hat{\mathbf{k}}_f \mid \varepsilon \mid^2 \tag{B.9}$$

where

$$1/\omega^*_{hf} = [1 + (3 + 4\, g_{F'})\, \beta/5\, \alpha]/\omega_6 - [1 - (1 - 12\, g_{F'})\, \beta/5\, \alpha]/\omega_7 . \tag{B.10}$$

In the case $H \geqslant \Delta H$, Hanle effect has to be applied to the spin polarization $\mathbf{P}^{(1)}_{hf}$ (defined in Eq. (B.9)) considered as the source term. The off-resonance contribution, from degeneracy lifting [37], is omitted in (B.9) in view of the minor rôle played by this signal in the PV experiment.

The implications of the effects described above are examined in section 1.3.1.

B.2 HANLE EFFECT ON POLARIZATIONS WHICH EXIST IN ZERO FIELD. — In the ideal configuration of the PV experiment (Sect. 1.2.3), the ξ-dependent PC components of the spin polarization are normal to the observation direction and thus undetected. Yet they are interesting for calibration or diagnostic purposes. Hanle effect in a magnetic field of suitable direction gives access to them. Since the corresponding signal is absent in zero magnetic field, it is contained in the H-odd part of the Hanle effect, which also offers the best experimental characterization. For a source polarization **P**, this part is simply (sgn g) $\mathcal{D}(H)\, \hat{\mathbf{H}} \times \mathbf{P}$, where $\mathcal{D}(H)$ is the Lorentz dispersion function :

$$\mathcal{D}(H) = (H/\Delta H)/[1 + (H/\Delta H)^2]; \tag{B.11}$$

ΔH is the Hanle width (Eq. (B.3)); $\hat{\mathbf{H}} = \mathbf{H}/H$. However, the collision-induced background introduced in appendix A (Eq. (A.21)) contributes too. It results from spin polarizations created in both hyperfine sublevels of the 7S state. Since these have opposite g-factors, they exhibit Hanle effects of opposite signs, so that partial compensation takes place. From (A.21), (A.8) and (B.11), their contribution to the polarized fluorescence signal, proportional to $\sum_{F'} n_{F'}\, p_{F'}(\operatorname{sgn} g_{F'}) = 2$, turns out to be independent of the nuclear spin. It is given by :

$$2\, B_p^2 \mid \varepsilon \mid^2 \mathcal{D}(H)\, \hat{\mathbf{H}} \times \xi\hat{\mathbf{k}} \cdot \xi_f\, \hat{\mathbf{k}}_f . \tag{B.12}$$

Finally, in the most general configuration, the H-odd, ξ-odd part of the polarized fluorescence signal is :

$$\begin{aligned}\mathcal{F}_p(H\text{-odd}, \xi\text{-odd}) = \{ &- n_{F'}\, p_{F'}(\operatorname{sgn} g_{F'})\, \delta_{FF'}\, \alpha\beta E^2 \cdot \hat{\mathbf{H}} \times \xi\hat{\mathbf{k}} + \\ &+ [n_{F'}\, p_{F'}(\operatorname{sgn} g_{F'})\, g_{FF'}\, M'^2_1 + 2\, B_p^2] \cdot \hat{\mathbf{H}} \times \xi\hat{\mathbf{k}} + \\ &+ n_{F'}\, p_{F'}(\operatorname{sgn} g_{F'})\, (\delta_{FF'}\, \alpha + g_{FF'}\, \beta)\, \beta(\mathbf{E} \cdot \xi\hat{\mathbf{k}}) \cdot \hat{\mathbf{H}} \times \mathbf{E} \} \cdot \xi_f\, \hat{\mathbf{k}}_f \mid \varepsilon \mid^2 \mathcal{D}(H) .\end{aligned} \tag{B.13}$$

We now apply this result to two particular cases of practical interest.

a) *Calibration of spin polarization measurements.* — We assume here the ideal configuration of the PV experiment (Sect. 1.2.3) i.e. $\hat{\mathbf{E}} \perp \hat{\mathbf{k}}$ and $\hat{\mathbf{k}}_f = \hat{\mathbf{E}} \times \hat{\mathbf{k}}$. But for possible small misalignments (considered in part II), the last of the three terms in (B.13) vanishes. In a $\Delta F = 0$ transition ($\delta_{FF'} = 1$), for a realistic value of E (typically 100 V/cm), the second term is only 1 % of the first one, which is the term of interest. To eliminate comple-

tely the small second term, we take for calibration signal the quantity :

$$\mathcal{F}_{cal} = \mathcal{F}_p(H\text{-odd}, \xi\text{-odd}, E) - \mathcal{F}_p(H\text{-odd}, \xi\text{-odd}, E = 0).$$

This quantity is finally equal to

$$\mathcal{F}_{cal} = n_{F'} p_{F'} (\text{sgn } g_{F'}) (-\delta_{FF'} \alpha\beta E^2) \mid \varepsilon \mid^2 \mathcal{D}(H_0) \hat{\mathbf{H}}_0 \times \xi\hat{\mathbf{k}} \cdot \xi_f \hat{\mathbf{k}}_f . \quad \text{(B.14)}$$

This formula is valid for any $\mathbf{H}_0$. In practice, to maximize the last factor, we take $\mathbf{H}_0$ normal to both $\hat{\mathbf{k}}$ and $\hat{\mathbf{k}}_f$, i.e. $\mathbf{H}_0 /\!/ \mathbf{E}$ (cf. Fig. 6) and $H_0 = \Delta H$, i.e. $\mathcal{D}(H_0) = 1/2$. The notation H_0 is used as a means of recalling this particular configuration :

$$(\hat{\mathbf{H}}_0, \hat{\mathbf{k}}, \hat{\mathbf{k}}_f) = \pm 1 .$$

b) *Measurement of* $\hat{\mathbf{E}} \cdot \hat{\mathbf{k}}$. — We assume again $\hat{\mathbf{k}}_f \perp \hat{\mathbf{k}}$, but $\hat{\mathbf{E}}$ can now take on any direction. We are interested in singling out the last term of (B.13) to measure $\hat{\mathbf{E}} \cdot \hat{\mathbf{k}}$. This is obtained by simply applying a magnetic field $\mathbf{H}$ along $\hat{\mathbf{k}}$, which cancels the two other terms in (B.13).

Appendix C.

This appendix completes § 2.10 by giving the complete expression of the quantity $\mathcal{A}^{pv}/C$ (Eqs. (2.9)-(2.11)) measured in each of both hfs components assuming perfect geometry (Fig. 6). We derive the expressions relevant for a single pass of the beam. (The effect of the multipass is to amplify the signals by the same factor which is eliminated in the normalization). We use the coordinate axes of figure 6 with $\hat{\mathbf{k}} = \hat{\mathbf{z}}$, $\hat{\mathbf{k}}_f = \hat{\mathbf{x}}$ and the following sign conventions :

$$\begin{aligned} \mathbf{E} &= \eta \mid \mathbf{E} \mid \hat{\mathbf{y}}, \qquad \eta = \pm 1, \\ \mathbf{H}_0 &= \eta'' \mid \mathbf{H}_0 \mid \hat{\mathbf{y}}, \qquad \eta'' = \pm 1. \end{aligned} \quad \text{(C.1)}$$

(i) Inserting equation (2.8) in (A.16), we obtain the PV amplitudes measured in zero magnetic field :

$$\mathcal{F}_{e\pm f} = \frac{1}{2} p_{F'} n_{F'} (\delta_{FF'} \alpha + g_{FF'} \beta) \mid \mathbf{E} \mid \text{Im } E_1^{pv} . \eta\eta' . \quad \text{(C.2)}$$

(ii) Inserting (2.8) in (B.14) and using (B.11), we obtain the calibration amplitudes measured in the $4 \to 4$ component, in a field $\mid \mathbf{H}_0 \mid = \Delta H$:

$$\mathcal{F}_{e\pm f}(H_0 = \Delta H) = -\frac{1}{4} n_{F'} p_{F'} (\text{sgn } g_{F'}) \alpha\beta E^2 . \eta\eta'' . \quad \text{(C.3)}$$

(iii) From equations (A.20), (2.3) and (2.5), the amplitude used for the normalization is written :

$$\mathcal{F}_{e+b} = \frac{1}{4} n_{F'} (\delta_{FF'} \alpha^2 - h_{FF'} \beta^2) E^2 . \quad \text{(C.4)}$$

Inserting now (C.2) and (C.4) in the definition of the experimental asymmetry (Eq. (2.9)), we obtain :

$$\mathcal{A}^{pv}_{FF'} = 4 p_{F'} \frac{\delta_{FF'} \alpha + g_{FF'} \beta}{\mid \delta_{FF'} \alpha^2 - h_{FF'} \beta^2 \mid} \frac{\text{Im } E_1^{pv}}{\mid E \mid}, \quad \text{(C.5a)}$$

and from the definition of the angular factors (Eqs. (A.8))

$$\mathcal{A}^{pv}_{4\to4} = \frac{5}{3} \frac{\text{Im } E_1^{pv}}{\alpha \mid E \mid} \left(1 + \frac{\beta}{8\alpha}\right) \left(1 - \frac{5\beta^2}{12\alpha^2}\right)^{-1}, \quad \text{(C.5b)}$$

$$\mathcal{A}^{pv}_{3\to4} = \frac{5}{2} \frac{\text{Im } E_1^{pv}}{\beta \mid E \mid} . \quad \text{(C.5c)}$$

Inserting (C.3) and (C.4) in the quantity C defined by Eq. (2.10), and using equations (A.6) for $F = F' = 4$, we obtain :

$$C_{4\to4} = -\frac{5}{6} \frac{\beta}{\alpha} \left(1 - \frac{5\beta^2}{12\alpha^2}\right)^{-1} . \quad \text{(C.6)}$$

The PV parameters finally extracted in each case are respectively :

$$\mathcal{A}^{pv}_{4\to4}/C_{4\to4} = -2 \frac{\text{Im } E_1^{pv}}{\beta \mid E \mid} \left(1 + \frac{\beta}{8\alpha}\right), \quad \text{(C.7a)}$$

$$\mathcal{A}^{pv}_{3\to4}/C_{4\to4} = -3 \frac{\text{Im } E_1^{pv}}{\beta \mid E \mid} \frac{\alpha}{\beta} \left(1 - \frac{5\beta^2}{12\alpha^2}\right). \quad \text{(C.7b)}$$

They are predicted to be of opposite signs since α/β has been observed to be negative [45]. Note that the absolute signs in (C.7) result from the sign convention (C.1).

References

[1] GLASHOW, S. L., *Nucl. Phys.* **22** (1961) 579 ;
WEINBERG, S., *Phys. Rev. Lett.* **19** (1967) 1264 ;
SALAM, A., Elem. Part. Theory, Proc. Nobel Symp., 8th (1968) 367 ;
HOOFT, G. T., *Nucl. Phys. B* **33** (1971) 173 ; and *B* **35** (1971) 167.

[2] DAVIER, M., *J. Physique Colloq.* **43** (1982) C3-471.

[3] BOUCHIAT, M. A. and BOUCHIAT, C., *Phys. Lett. B* **48** (1974) 111.

[4] BOUCHIAT, M. A. and BOUCHIAT, C., *J. Physique* **35** (1974) 899.

[5] BOUCHIAT, M. A., GUENA, J., HUNTER, L. and POTTIER, L., *Phys. Lett. B* **117** (1982) 358.

[6] BOUCHIAT, M. A., GUENA, J., HUNTER, L. and POTTIER, L., *Phys. Lett. B* **134** (1984) 463.

[7] FORTSON, E. N. and LEWIS, L. L., *Phys. Rep.* **113** (1984) 289 ;
BOUCHIAT, M. A. and POTTIER, L., in *Atomic Physics 9*, eds. R. S. van Dyck Jr. and E. N. Fortson, World Scientific (Singapore) 1984 ;
BARKOV, L. M., ZOLOTOREV, M. D. and KHRIPLOVICH, I. B., *Sov. Phys. Usp.* **23** (1980) 713.

[8] BAIRD, P. E. G. *et al.*, *Nature* **264** (1976) 528 ;
LEWIS, L. L. *et al.*, *Phys. Rev. Lett.* **39** (1977) 795 ;
BAIRD, P. E. G. *et al.*, *Phys. Rev. Lett.* **39** (1977) 798 ;
FORTSON, E. N., *Neutrinos-78*, E. Fowler Ed., p. 417.

[9] BARKOV, L. M. and ZOLOTOREV, M. S., *JETP Lett.* **27** (1978) 357 and *Phys. Lett. B* **85** (1979) 308.

[10] BOGDANOV, Yu. V. *et al.*, *JETP Lett.* **31** (1980) 214 and 522.

[11] HOLLISTER, J. H. *et al.*, *Phys. Rev. Lett.* **46** (1981) 643.

[12] THOMPSON, R. C., Les Houches, Session XXXVIII (1982), *New trends in atomic physics*, G. Grynberg and R. Stora Eds (Elsevier) 1984.

[13] SOBEL'MAN, I. I., Private communication ; BIRICH, G. N. *et al.*, *Zh. Eksp. & Teor. Fiz.* **87** (1984) 776.

[14] EMMONS, T. P., REEVES, J. M. and FORTSON, E. N., *Phys. Rev. Lett.* **51** (1983) 2089.

[15] BUCKSBAUM, P., COMMINS, E. and HUNTER, L., *Phys. Rev. Lett.* **46** (1981) 640.

[16] DRELL, P. S. and COMMINS, E. D., *Phys. Rev. Lett.* **53** (1984) 968.

[17] FLAMBAUM, V. V., KHRIPLOVICH, I. B. and SUSHKOV, O. P., *Phys. Lett.* **67A** (1978) 177.

[18] DZUBA, V. A., FLAMBAUM, V. V., SILVESTROV, P. G. and SUSHKOV, O. P., preprint (1984), submitted to Phys. Scr.

[19] BOUCHIAT, M. A., GUENA, J. and POTTIER, L., *J. Physique Lett.* **45** (1984) L-61.

[20] GILBERT, S. L., WATTS, R. N. and WIEMAN, C. E., *Phys. Rev.* **A 29** (1984) 137.

[21] BOUCHIAT, M. A., GUENA, J., POTTIER, L., *Opt. Commun.* **51** (1984) 243.

[22] BOUCHIAT, M. A. et BOUCHIAT, C., *J. Physique* **36** (1975) 493.

[23] BOUCHIAT, C., PIKETTY, C. A. and PIGNON, D., *Nucl. Phys.* **B 221** (1983) 68.

[24] MARCIANO, W. J. and SIRLIN, A., *Phys. Rev.* **D 27** (1983) 552 ;
LYNN, B. W., in : 1983 Trieste Conf. on Radiative Corrections in SU2XU1, p. 311, B. W. Lynn and J. F. Wheater eds (World Scientific, Singapore) 1984.

[25] DAS, B. P. *et al.*, preprint (1982), State University of New York, Albany, N.Y., USA.

[26] DZUBA, V. A., FLAMBAUM, V. V., SILVESTROV, P. G. and SUSHKOV, O. P., *J. Phys. B* **18** (1985) 597.

[27] MÅRTENSSON, A.-M., abstract B96, 9th ICAP, Seattle (1984), R. S. Van Dyck and E. N. Fortson eds, unpublished.

[28] HOFFNAGLE, J., TELEGDI, V. L. and WEIS, A., *Phys. Lett.* **86A** (1981) 457 ;
HOFFNAGLE, J., Dissertation (n° 6999), Swiss Federal Institute of Technology, Zürich (Switzerland, 1982), unpublished.

[29] SHABANOVA, L. N., MONAKOV, Y. N. and KHLYUSTALOV, A. N., *Opt. Spect.* **47** (1979) 1.

[30] BOUCHIAT, M. A., GUENA, J. and POTTIER, L., *J. Physique Lett.* **45** (1984) L-523.

[31] WATTS, R. N., GILBERT, S. L. and WIEMAN, C. E., *Phys. Rev.* **A 27** (1983) 2769.

[32] BOUCHIAT, M. A., GUENA, J., HUNTER, L. and POTTIER, L., *Opt. Commun.* **45** (1983) 35.

[33] HOFFNAGLE, J., ROESCH, L. Ph., TELEGDI, V. L., WEIS, A. and ZEHNDER, A., *Phys. Lett.* **85A** (1981) 143.

[34] GILBERT, S. L., WATTS, R. N. and WIEMAN, C. E., *Phys. Rev.* **A 27** (1983) 581.

[35] ARIMONDO, E., INGUSCIO, M. and VIOLINO, P., *Rev. Mod. Phys.* **49** (1977) 31.

[36] MOLOF, R. W. *et al.*, *Phys. Rev.* **A 10** (1974) 1131.

[37] BOUCHIAT, M. A. and POIRIER, M., *J. Physique* **43** (1982) 729 ;
POIRIER, M., Thèse de 3e cycle, Paris VI Univ. (1979) unpublished.

[38] BOUCHIAT, M. A., GUENA, J., HUNTER, L. and POTTIER, L., *Opt. Commun.* **46** (1983) 185.

[39] BOUCHIAT, M. A., CLOUQUEUR, A., POTTIER, L., *Revue Phys. Appl.* **15** (1980) 1275.

[40] BOUCHIAT, M. A. and POTTIER, L., *Opt. Commun.* **37** (1981) 229.

[41] HERRIOT, D., KOGELNIK, H. and KOMPFNER, R., *Appl. Opt.* **3** (1964) 523.

[42] BOUCHIAT, M. A., POTTIER, L. and TRENEC, G., *Revue Phys. Appl.* **15** (1980) 785.

[43] BOUCHIAT, M. A., COBLENTZ, A., GUENA, J., POTTIER, L., *J. Physique* **42** (1981) 985.

[44] BOUCHIAT, M. A., POTTIER, L., *Appl. Phys.* **B 29** (1982) 43.

[45] BOUCHIAT, M. A., GUENA, J., POTTIER, L., *Opt. Commun.* **37** (1981) 265.